BRAIN
ORIGINAL ARTICLE

Biallelic null variants in *PNPLA8* cause microcephaly by reducing the number of basal radial glia

Yuji Nakamura,[1] Issei S. Shimada,[2,†] Reza Maroofian,[3] Micol Falabella,[3] Maha S. Zaki,[4] Masanori Fujimoto,[1] Emi Sato,[1] Hiroshi Takase,[5] Shiho Aoki,[6] Akihiko Miyauchi,[6] Eriko Koshimizu,[7] Satoko Miyatake,[7,8] Yuko Arioka,[9] Mizuki Honda,[10,11] Takayoshi Higashi,[12] Fuyuki Miya,[13] Yukimune Okubo,[14] Isamu Ogawa,[15] Annarita Scardamaglia,[3] Mohammad Miryounesi,[16] Sahar Alijanpour,[16] Farzad Ahmadabadi,[17] Peter Herkenrath,[18] Hormos Salimi Dafsari,[18,19,20] Clara Velmans,[21] Mohammed Al Balwi,[22] Antonio Vitobello,[23,24] Anne-Sophie Denommé-Pichon,[23,24] Médéric Jeanne,[25,26] Antoine Civit,[25] Mohamed S. Abdel-Hamid,[27] Hamed Naderi,[28] Hossein Darvish,[28] Somayeh Bakhtiari,[29,30] Michael C. Kruer,[29,30] Christopher J. Carroll,[31] Ehsan Ghayoor Karimiani,[31] Rozhgar A. Khailany,[32] Talib Adil Abdulqadir,[33] Mehmet Ozaslan,[34] Peter Bauer,[35] Giovanni Zifarelli,[35] Tahere Seifi,[36,37] Mina Zamani,[36,37] Chadi Al Alam,[38] Javeria Raza Alvi,[39] Tipu Sultan,[3] Stephanie Efthymiou,[3] Simon A. S. Pope,[40,41] Kazuhiro Haginoya,[14] Tamihide Matsunaga,[15] Hitoshi Osaka,[6] Naomichi Matsumoto,[7] Norio Ozaki,[9] Yasuyuki Ohkawa,[42] Shinya Oki,[10,43] Tatsuhiko Tsunoda,[44,45,46] Robert D. S. Pitceathly,[3,47] Yoshitaka Taketomi,[12] Henry Houlden,[3] Makoto Murakami,[12] Yoichi Kato[2,†] and Shinji Saitoh[1,†]

[†]These authors contributed equally to this work.

Patatin-like phospholipase domain-containing lipase 8 (PNPLA8), one of the calcium-independent phospholipase A_2 enzymes, is involved in various physiological processes through the maintenance of membrane phospholipids. Biallelic variants in *PNPLA8* have been associated with a range of paediatric neurodegenerative disorders. However, the phenotypic spectrum, genotype–phenotype correlations and the underlying mechanisms are poorly understood. Here, we newly identified 14 individuals from 12 unrelated families with biallelic ultra-rare variants in *PNPLA8* presenting with a wide phenotypic spectrum of clinical features. Analysis of the clinical features of current and previously reported individuals (25 affected individuals across 20 families) showed that *PNPLA8*-related neurological diseases manifest as a continuum ranging from variable developmental and/or degenerative epileptic–dyskinetic encephalopathy to childhood-onset neurodegeneration. We found that complete loss of PNPLA8 was associated with the more profound end of the spectrum, with congenital microcephaly.

Using cerebral organoids generated from human induced pluripotent stem cells, we found that loss of PNPLA8 led to developmental defects by reducing the number of basal radial glial cells and upper-layer neurons. Spatial

Received May 18, 2023. Revised May 05, 2024. Accepted May 20, 2024. Advance access publication July 31, 2024

transcriptomics revealed that loss of PNPLA8 altered the fate specification of apical radial glial cells, as reflected by the enrichment of gene sets related to the cell cycle, basal radial glial cells and neural differentiation. Neural progenitor cells lacking PNPLA8 showed a reduced amount of lysophosphatidic acid, lysophosphatidylethanolamine and phosphatidic acid. The reduced number of basal radial glial cells in patient-derived cerebral organoids was rescued, in part, by the addition of lysophosphatidic acid.
Our data suggest that PNPLA8 is crucial to meet phospholipid synthetic needs and to produce abundant basal radial glial cells in human brain development.

1 Department of Pediatrics and Neonatology, Nagoya City University Graduate School of Medical Sciences, Nagoya 4678601, Japan
2 Department of Cell Biology, Nagoya City University Graduate School of Medical Sciences, Nagoya 4678601, Japan
3 Department of Neuromuscular Diseases, UCL Queen Square Institute of Neurology, University College London, London WC1N 3BG, UK
4 Clinical Genetics Department, Human Genetics and Genome Research Institute, National Research Centre, Cairo 12622, Egypt
5 Core Laboratory, Nagoya City University Graduate School of Medical Sciences, Nagoya 4678601, Japan
6 Department of Pediatrics, Jichi Medical University, Tochigi 3290498, Japan
7 Department of Human Genetics, Yokohama City University Graduate School of Medicine, Yokohama 2360004, Japan
8 Department of Clinical Genetics, Yokohama City University Hospital, Yokohama 2360004, Japan
9 Pathophysiology of Mental Disorders, Nagoya University Graduate School of Medicine, Nagoya 4668550, Japan
10 Department of Drug Discovery Medicine, Kyoto University Graduate School of Medicine, Kyoto 6068507, Japan
11 Laboratory of Molecular and Cellular Physiology, Graduate School of Integrated Sciences for Life, Hiroshima University, Hiroshima 7398526, Japan
12 Laboratory of Microenvironmental and Metabolic Health Sciences, Center for Disease Biology and Integrative Medicine, Graduate School of Medicine, The University of Tokyo, Tokyo 1138655, Japan
13 Center for Medical Genetics, Keio University School of Medicine, Tokyo, 1608582, Japan
14 Department of Pediatric Neurology, Miyagi Children's Hospital, Sendai 9893126, Japan
15 Department of Clinical Pharmacy, Graduate School of Pharmaceutical Sciences, Nagoya City University, Nagoya 4678603, Japan
16 Department of Medical Genetics, Faculty of Medicine, Shahid Beheshti University of Medical Sciences, Tehran 1516745811, Iran
17 Pediatric Neurology Department, Faculty of Medicine, Mofid Children's Hospital, Shahid Beheshti University of Medical Sciences, Tehran 1546815514, Iran
18 Department of Pediatrics and Center for Rare Diseases, Faculty of Medicine and University Hospital Cologne, University of Cologne, Cologne 50937, Germany
19 Max-Planck-Institute for Biology of Ageing, Cologne 50931, Germany
20 Cologne Excellence Cluster on Cellular Stress Responses in Aging-Associated Diseases (CECAD), University of Cologne, Cologne 50931, Germany
21 Faculty of Medicine and University Hospital Cologne, Institute of Human Genetics, University of Cologne, Cologne 50931, Germany
22 Department of Pathology and Laboratory Medicine, College of Medicine, KSAU-HS, Ministry of National Guard Health Affairs, Riyadh 11426, Saudi Arabia
23 Functional Unit for Diagnostic Innovation in Rare Diseases, FHU-TRANSLAD, Dijon Bourgogne University Hospital, Dijon 21000, France
24 INSERM UMR1231 GAD 'Génétique des Anomalies du Développement', FHU-TRANSLAD, University of Burgundy, Dijon 21000, France
25 Genetics Department, University Hospital of Tours, Tours 37044, France
26 UMR 1253, iBrain, University of Tours, INSERM, Tours 37032, France
27 Medical Molecular Genetics Department, Human Genetics and Genome Research Institute, National Research Centre, Cairo 12622, Egypt
28 Neuroscience Research Center, Faculty of Medicine, Golestan University of Medical Sciences, Gorgan 4918936316, Iran
29 Pediatric Movement Disorders Program, Division of Pediatric Neurology, Barrow Neurological Institute, Phoenix Children's Hospital, Phoenix, AZ 85016, USA
30 Departments of Child Health, Neurology, Cellular & Molecular Medicine and Program in Genetics, University of Arizona College of Medicine, Phoenix, AZ 85004, USA
31 Genetics Section, Molecular and Clinical Sciences Research Institute, St. George's, University of London, London SW17 0RE, UK

32 Department of Basic Science, Hawler Medical University, Erbil, Kurdistan Region 44001, Iraq
33 Department of Pediatrics, College of Medicine, Hawler Medical University, Erbil, Kurdistan Region 44001, Iraq
34 Department of Biology, Division of Molecular Biology and Genetics, Gaziantep University, Gaziantep 27410, Turkey
35 Centogene GmbH, Rostock 18055, Germany
36 Department of Biology, Faculty of Science, Shahid Chamran University of Ahvaz, Ahvaz 83151-61355, Iran
37 Narges Medical Genetics and Prenatal Diagnosis Laboratory, Kianpars, Ahvaz 61556-89467, Iran
38 Pediatrics and Pediatric Neurology, American Center for Psychiatry and Neurology, Abu Dhabi 108699, UAE
39 Department of Pediatric Neurology, the Children's Hospital and the University of Child Health Sciences, Lahore 54600, Pakistan
40 Genetics and Genomic Medicine, UCL Great Ormond Street Institute of Child Health, London WC1N 1EH, UK
41 Neurometabolic Unit, The National Hospital for Neurology and Neurosurgery, London WC1N 3BG, UK
42 Division of Transcriptomics, Medical Institute of Bioregulation, Kyushu University, Fukuoka 8128582, Japan
43 Institute of Resource Development and Analysis, Kumamoto University, Kumamoto 8600811, Japan
44 Laboratory for Medical Science Mathematics, Department of Biological Sciences, School of Science, The University of Tokyo, Tokyo 113-0033, Japan
45 Laboratory for Medical Science Mathematics, Department of Computational Biology and Medical Sciences, Graduate School of Frontier Sciences, The University of Tokyo, Tokyo 113-0033, Japan
46 Laboratory for Medical Science Mathematics, RIKEN Center for Integrative Medical Sciences, Yokohama 230-0045, Japan
47 NHS Highly Specialised Service for Rare Mitochondrial Disorders, Queen Square Centre for Neuromuscular Diseases, The National Hospital for Neurology and Neurosurgery, London WC1N 3BG, UK

Correspondence to: Issei S. Shimada
Department of Cell Biology, Nagoya City University
Graduate School of Medical Sciences, Kawasumi 1
Mizuho-cho, Mizuho-ku, Nagoya 467-8601, Japan
E-mail: ishimada@med.nagoya-cu.ac.jp

Correspondence may also be addressed to: Yoichi Kato
E-mail: kato.41@med.nagoya-cu.ac.jp

Correspondence may also be addressed to: Shinji Saitoh
Department of Pediatrics and Neonatology, Nagoya City University
Graduate School of Medical Sciences, Kawasumi 1
Mizuho-cho, Mizuho-ku, Nagoya, 467-8601, Japan
E-mail: ss11@med.nagoya-cu.ac.jp

Keywords: iPLA$_2$γ; brain organoid; outer radial glia; developmental encephalopathy

Introduction

In the evolutionarily expanded cerebral cortex, the increased proliferation of neural stem and progenitor cells (NPCs) underlies the increased number of neurons.[1] Basal radial glial cells (bRGCs) are a distinct type of NPC and are characterized by a significant proliferative potential compared with the other types of NPCs.[2-4] BRGCs originate from apical radial glial cells (aRGCs). When aRGCs divide, they produce diverse cell types other than bRGCs, such as aRGCs, neurons and basal intermediate progenitor cells (bIPs).[5] In contrast, most bRGCs undergo self-renewal divisions, leading to exponential amplification.[2] Therefore, the abundance of bRGCs has been linked to the highly expanded and folded cerebral cortex.[3] The difference in the number of bRGCs can result in a phenotypic discrepancy in mice and humans. For example, genetic variants in *WDR62* are a cause of congenital microcephaly with a reduced abundance of bRGCs,[6,7] but *Wdr62* mutant mice exhibit a milder microcephaly phenotype than humans.[7]

Patatin-like phospholipase domain-containing lipase 8 (PNPLA8), also called calcium-independent phospholipase A$_2$γ, is a phospholipase A$_2$ (PLA$_2$) enzyme conserved across species.[8-10] *PNPLA8* transcripts have multiple translation initiation sites, thereby expressing multiple protein sizes (molecular weights of 88, 77, 74 and 63 kDa).[11,12] PNPLA8 was shown to be expressed in distinct tissues, including the brain.[13] The subcellular localization of PNPLA8 is unique in that it has a mitochondrial localization sequence unlike other PNPLA family members sharing the common lipase consensus domain.[12] PNPLA8 hydrolyses phospholipids to generate lysophospholipids and free fatty acids, thereby regulating multiple cellular processes, namely membrane remodelling,[14-16] maintenance of mitochondrial function,[14,15,17] protection against oxidative stress[18,19] and lipid mediator biosynthesis.[20,21]

The loss of PNPLA8 function has been suggested to affect the CNS in mice and humans.[14,15,22-25] Neurodegenerative phenotypes were documented in *Pnpla8* knockout (KO) mice, because they exhibited spatial learning and memory deficits, with morphological alterations of mitochondria in the hippocampus, despite the gross anatomy of their brains appearing normal.[14] The initial case report on a human patient suggested that biallelic variants in *PNPLA8* cause childhood-onset neurodegeneration and/or myopathy as observed in *Pnpla8* KO mouse models.[24] However, subsequent clinical reports have raised the possibility of wider phenotypic variability ranging from adolescence-onset movement disorder to early-onset encephalopathy accompanied by congenital microcephaly.[22,23,25-27]

Although the clinical features have not been detailed fully owing to the small number of patients, the possible occurrence of congenital microcephaly[24] underscores the importance of elucidating unknown roles of PNPLA8 in human brain development.

Here, we report 14 individuals showing neurological manifestations from 12 unrelated families with biallelic variants in *PNPLA8*. We describe a human cerebral organoid model lacking *PNPLA8* to investigate the loss-of-function (LoF) nature of *PNPLA8* variants specifically in cortical development. We explore the disease mechanism further with multi-omics approaches. Our data detail the clinical features and indicate that a complete loss of PNPLA8 impairs bRGC-mediated cortical expansion in humans.

Materials and methods

Additional details can be found in the Supplementary material, Methods.

Study approval

Genetic and functional analysis using samples from study participants was approved by the institutional review boards at Nagoya City University (approval number: 70-00-0200), Yokohama City University (approval number: A170525011) and University College London (approval number: #310045/1571740/37/598). Parents and legal guardians of all affected individuals consented to the publication of clinical and genetic information, including video and photographs, and the study was approved by the respective local ethics committees. The generation and application of the induced pluripotent stem cells (iPSCs) were approved by the Nagoya University Ethics Committee (approval number: 2012-0184) and Nagoya City University Ethics Committee (approval number: 19-143). Written informed consent was obtained from the guardians of patients. The analysis using skin fibroblasts derived from the patient with Leigh syndrome was approved by the institutional review board at Jichi Medical University (approval number: J21-014).

Patients

Sixteen individuals from 14 unrelated families from around the world were identified through international collaboration and data sharing. Although Families 7 and 8 in this study had been previously reported without details,[22,28] we included these patients with unreported clinical and genetic data. Additionally, we reviewed the clinical features of previously reported patients[23-27,29] (Table 1). Physical features of weight and head circumference were converted to standard deviation (SD) scores, corrected for sex, age and gestational age.[30,31] Clinically acquired brain images were available for nine patients. Among them, only low-resolution photographs of brain MRIs were available for Patients 6, 8, 10 and 12.

Genetic analysis

Proband-only or trio-exome/genome sequencing and bioinformatics with subsequent candidate variant Sanger segregation analysis was carried out on DNA extracted from blood-derived leucocytes at different genetic diagnostic and research laboratories worldwide following slightly different protocols, as described previously.[32-34] Nucleotide sequences were described with reference to *PNPLA8* transcript NM_001256007.3.

Generation of *PNPLA8* knockout induced pluripotent stem cell lines

Previously established human iPSCs (Windy) were used in this study.[35-37] Clustered regularly interspaced short palindromic repeats (CRISPR)/Cas9-mediated genome editing in iPSCs was performed as previously described with modifications.[38] Further details are provided in the Supplementary material, Methods.

Generation of cerebral organoids from induced pluripotent stem cells

To generate *PNPLA8* KO cerebral organoids, we used a dual SMAD inhibitor protocol with slight modifications.[39,40] We seeded 3000 iPSCs into 96-well V-bottom plates and cultured them in the 'induction media' (Supplementary material, Methods) with 50 µM Y-27632 (for the first 48 h) for the first 6 days, with replacement every 2 days. On the sixth day in suspension, the spheroids were transferred into non-adherent 24-well plates, precoated with poly(2-hydroxyethyl methacrylate) solution (1.2 g of 2-hydroxyethyl methacrylate in 50 ml of 95% ethanol). The spheroids were then cultured in the 'organoid culture media 1' (Supplementary material, Methods), replaced every 2–3 days. The plates were rotated on an orbital shaker (CS-LR; TAITEC) at 70 rpm. To promote differentiation of the neural progenitors into neurons, the spheroids were cultured in 'organoid culture media 2' (Supplementary material, Methods) from Day 14 to 3 months. The culture medium was replaced every 1–3 days. After 1 month, the organoids were cut into two or three pieces with a scalpel under a stereo microscope (S6E; Leica) every week to prevent cell death in the central portions.[41]

Patient- and control-derived cerebral organoids were generated by a slightly different protocol. For embryoid body (EB) formation, we seeded 188 000 iPSCs into EZ-sphere 24-well plates (~400 cells per micro-well) and cultured them in the 'EB formation media' (Supplementary material, Methods) with 50 µM Y-27632 (for the first 48 h). On the third day, the culture medium was changed to 'induction media' until the sixth day, with replacement every 2 days. On the sixth day, the culture medium was removed, and EB spheroids were embedded in 200 µl of cold Matrigel and incubated at 37°C for 30 min. Subsequently, 1 ml of 'organoid culture media 1' was added to the culture plates. On the 10th day, the cerebral organoids were transferred into six-well 2-hydroxyethyl methacrylate-coated plates on an orbital shaker at 70 rpm. On the 14th day, culture medium was replaced with 'organoid culture media 2'. The cerebral organoids were cultured for ≤2 months. The culture medium was replaced every 1–3 days. After 1 month, the organoids were cut into two or three pieces with a scalpel under a stereo microscope every week to prevent cell death in the central portions.[41] For bromodeoxyuridine (BrdU) labelling, cerebral organoids were treated with 10 µM BrdU for 24 h, then fixed for analysis. For treatment with lysophosphatidic acid (LPA), 3 µM LPA was added to the medium at the beginning of the eighth week of culture. Medium was changed daily, and organoids were fixed for analysis after 7 days of treatment.

Images of the organoids were acquired using an inverted optical microscope (CKS53; Olympus). The organoid size was measured based on the surface of the organoids using ImageJ and FIJI software.

Spatial transcriptomic analysis

Cerebral organoids were fixed in 4% paraformaldehyde in PBS at room temperature (RT) for 10 min, followed by 30% sucrose in PBS

Table 1 Summary of clinical features for affected individuals with *PNPLA8* variants

Family	1	2	3	4	5	6	7[a]	8[a]	Shukla *et al.*[25]	Fields *et al.*[29]		Masih *et al.*[23]	Abdel-Hamid *et al.*[27]			9	Shukla *et al.*[25]	10	Saunders *et al.*[24]	Burnyte *et al.*[26]		11a	11b	11c	12
Sex	M	F	F	F	M	F	M	F	F	NA	M	F	F	F	F	M	F	F	F	M	F	M	M	F	F
Age at last assessment	4 y[b]	10 mo[b]	3 d	1 y	2 y	1 y	3 y	8 mo[b]	10 d	NA	NA	5 mo	2 mo[b]	1 y[b]	3 y	3 y	14 y	9 y	7 y	49 y	21 y	33 y	NA	29 y	21 y
Origin	JPN	JPN	SAU	IRQ	AFG	PAK	TUR	LBN	IND	NA	NA	IND	EGY	EGY	EGY	TUR	IND/FJI	EGY	NA	NA	NA	IRN	IRN	IRN	EGY
Consanguinity	–	–	+	+	+	+	+	+	+	NA	NA	+	+	+	+	+	–	+	NA	–	–	+	+	+	+
Congenital MIC	+	+	+	+	NA	–	–	+	+	+	+	+	NA	NA	+	+	–	–	–	NA	NA	NA	NA	NA	–
Progressive MIC	+	+	NA	+	+	+	+	+	NA	NA	NA	+	+	+	+	+	+	–	–	NA	NA	NA	NA	NA	–
DD	+	+	NA	+	+	+	+	+	NA	NA	NA	+	+	+	+	+	–	–	–	–	–	–	–	–	+
Milestones	No	No	NA	No	No	No	No	No	NA	NA	NA	No	No	HC	HC	No	ST	WK	WK	WK	WK	WK	WK	WK	WK
Regression	–	–	NA	–	–	–	–	–	NA	NA	NA	–	–	+	+	–	+	+	+	+	+	+	+	+	+
ID	Sev	Sev	NA	Sev	Sev	Sev	Sev	NA	NA	NA	NA	Sev	Sev	Sev	Sev	Sev	NA	–	NA	–	–	–	–	–	Mild
Hypotonia	+	+	NA	+	+	+	+	+	NA	NA	NA	NA	NA	NA	NA	+	+	+	+	–	–	+	+	+	+
Spasticity	+	+	+	+	+	–	+	+	+	NA	NA	+	+	+	+	–	+	+	+	–	–	–	–	–	–
Dystonia	+	+	NA	–	–	–	–	NA	NA	NA	NA	NA	+	NA	NA	+	+	+	+	NA	NA	+	+	+	+
Ataxia	NA	NA	NA	NA	NA	–	–	NA	NA	NA	NA	NA	NA	NA	NA	–	NA	+	NA	+	+	+	+	+	–
NeuroMD	–	–	–	–	–	–	–	–	–	NA	NA	–	–	–	–	+	+	+	+	+	+	+	+	+	+
Seizure, AAO	1 d	1 d	1 d	7 mo	3 mo	2 d	1 mo	1 d	2 d	1 d	1 d	1 d	<1 mo	7 mo	1 y	2 y	1 y	–	7 y	–	–	–	31 y	–	–
Simplified gyri	+	+	+	NA	NA	+	+	+	+	+	NA	+	–	–	–	–	–	–	–	–	NA	–	NA	–	–
PCH	+	+	+	NA	+	+	+	+	+	NA	NA	+	+	+	+	+	+	–	–	–	NA	–	NA	–	–
CA	+	+	NA	+	+	NA	+	NA	NA	NA	NA	+	+	+	+	NA	+	–	–	–	NA	–	NA	–	–
CbA	+	+	+	NA	+	+	+	+	+	+	NA	+	+	+	+	+	+	+	–	+	NA	+	NA	+	+

AAO = age at onset; CA = cerebral atrophy; CbA = cerebellar atrophy; d = day; DD = developmental delay; F = female; HC = head control; ID = intellectual disability; M = male; MIC = microcephaly; mo = month; NA = not available; NeuroMD = neuromuscular disorder; PCH = pontocerebellar hypoplasia; Sev = severe; ST = stand; WKv walk; y = year. Origin: AFG = Afghanistan; EGY = Egypt; FJI = Fiji; IND = India; IRN = Iran; IRQ = Iraq; JPN = Japan; LBN = Lebanon; PAK = Pakistan; SAU, = Saudi Arabia; TUR = Turkey.

[a]Additional data to the previously reported cases by Denommé-Pichon *et al.*[28] (Family 7) and Harmouch *et al.*[22] (Family 8).

[b]Age at the time of their death.

at 4°C for 24 h. The organoids were transferred into Tissue-Tek O.C.T. compound, rapidly frozen in dry ice-cooled 2-methylbutane, and kept frozen at −80°C. Subsequently, 10-μm thick sections were obtained using a cryostat. Spatial transcriptomic analysis using the photo-isolation chemistry technique was performed as previously described.[42,43] Briefly, reverse transcription was performed by adding ultraviolet (UV)-responsive 6-nitropiperonyloxymethyl-caged reverse transcription primers containing T7 promotor, unique molecular identifiers (UMIs), multiple barcodes and polyT sequence onto the organoid sections. Immunofluorescence was then performed to visualize regions of interest (ROIs) for subsequent UV irradiation. To cleave 6-nitropiperonyloxymethyl moieties from reverse transcription primers, the ROIs were irradiated with UV light for 15 min with a Digital Micromirror Device (Polygon 1000-G; Mightex Systems). The total tissue lysate was then collected and purified using 20 mg/ml proteinase K. Second-strand DNA was synthesized by the nick translation method. For *in vitro* transcription reaction, synthesized cDNAs were transcribed to RNAs using a T7 Transcription Kit. After the collection of ROI-specific RNAs, the RNAs were further reverse transcribed, followed by paired-end sequencing on the Illumina platform (Read 1, UMIs and barcode; Read 2, cDNA). Sequences were separated by the sample barcodes with UMI-tools and mapped to the reference genome using HISAT2. UMI-tools and featureCounts were used to generate UMI count data assigned to genes. Differentially expressed genes (DEGs) were extracted by DESeq2 [false discovery rate (FDR) = 0.1]. The DEGs were filtered further with adjusted *P*-values < 0.1. DESeq2 was also used to transform the count data into regularized log data before performing principal component analysis using the R prcomp function. Enrichment maps were constructed with Cytoscape 3.9 and the BiNGO plug-in using the default settings.[44] The degree of enrichment for each gene ontology (GO) was assessed and considered significant when $P < 0.05$. Gene set enrichment analysis (GSEA) was performed on normalized counts of RNA-seq datasets. Enrichment *P*-values were estimated by 1000 permutations. The gene set databases used were Curated (C2; $n = 6449$), Hallmark (H; $n = 50$), Gene Ontology (GO) (C5; $n = 15\,703$) and Pathway Interaction Database (C2; PID; $n = 196$) gene set collections.[45-48] Specifically, GO results were visualized using the Enrichment Map plug-in for Cytoscape v.3.9 (*P*-value < 0.005, FDR *q*-value < 0.05). Clusters of functionally related enriched GO terms with at least five nodes were detected manually.

Lipidomic analysis

Lipidomic analysis was performed by electrospray ionization-liquid chromatography–mass spectrometry/mass spectrometry according to a published protocol.[49] Total lipids from cell lysate were extracted by the method of Bligh and Dyer.[50] To determine the amount of each phospholipid, lipid phosphorus was measured by Bartlett's method.[51] The analysis of phospholipid species was performed using a hybrid triple quadrupole–linear ion trap mass spectrometer (4500Q-TRAP; AB Sciex) with Nexera ultra-performance liquid chromatography (UPLC) system (Shimazu). As internal standards, a phospholipid mixture containing 12.5 pmol of each phospholipid [phosphatidylcholine (PC) 25:0, phosphatidylethanolamine (PE) 25:0, phosphatidylglycerol (PG) 25:0, phosphatidylinositol (PI) 25:0, phosphatidylserine (PS) 25:0 and phosphatidic acid (PA) 34:0], 25 pmol of each lysophospholipid [lysophosphatidylcholine (LPC)-d49 16:0, lysophosphatidylethanolamine (LPE)-d7 18:1, lysophosphatidylglycerol (LPG) 17:1, lysophosphatidylserine (LPS) 17:1], 250 pmol of lysophosphatidylinositol (LPI) 17:1, 75 pmol of LPA 17:0 and 10 pmol of cardiolipin (CL) 56:0 was added to each sample. For the analysis of free fatty acids, 12.5 pmol of arachidonic acid-d8 was added to each sample as an internal standard. Samples (1 or 3 nmol) were injected by an autosampler and separated using an Acquity UPLC HSS T3 column (Waters) or SeQuant ZIC-HILIC column (Merck Millipore). Data were acquired using Analyst (Sciex) and processed using MultiQuant software (Sciex). Lipid peaks were identified according to retention times and multiple reaction monitoring transitions and they were quantified relative to the internal standard using the peak area ratio method.

Statistics

Quantitative data were generated in at least three independent experiments. All data are expressed as the mean ± SD or standard error of the mean (SEM), as indicated in the figure legends. Significant differences between two groups were assessed by Student's unpaired *t*-test with Welch's correction. Other statistical analyses were performed using one-way ANOVA followed by Dunnett's multiple comparisons. All statistical analyses were done using Graph-pad Prism9 software (GraphPad Software, USA). *P*-values of <0.05 indicated a significant difference between groups. In organoid experiments for quantifying specific area or the number of cells, *n* represents the number of individual cortical units (the number of organoids tested is specified in figure legends). Organoid and NPC experiments were performed on biological replicates. For each independent experiment, the samples were generated anew from distinct passages of each iPSC line. The measurement of mitochondrial oxidative phosphorylation (OXPHOS) using skin fibroblasts was performed on technical replicates from the Patient 1 sample ($n = 1$).

Results

General characterization of biallelic variants in *PNPLA8*

We identified 14 individuals (six male and eight female individuals) showing neurological manifestations from 12 unrelated families with biallelic variants in *PNPLA8* (Fig. 1A). The age of the patients at the last assessment ranged from 3 days to 33 years of age (Table 1). We identified 14 variants, of which 12 were novel. Of the 14 variants, four were nonsense, five were frameshift, three were intronic variants near an exon–intron boundary, and two were missense variants. According to the population-based variant frequency data, such as the Single Nucleotide Polymorphism database,[52] 1000Genomes,[53] jMorp[54] and the Genome Aggregation Database,[55] the frequency of all of the variants was <0.001%, suggesting a strong purification effect attributable to disease pathogenicity.

Regarding the impact on splicing, c.1625+3_1625+6del identified in the patient from Family 1 (Patient 1) was assessed using patient blood-derived lymphoblastoid cell lines. Sequencing of each separated transcript by TA cloning revealed that c.1625+3_1625+6del resulted in the skipping of exons 6–8 owing to aberrant splicing (Supplementary Fig. 1A and B). Immunoblotting analysis for the skin fibroblasts from Patient 1 showed a significant reduction in 77-kDa PNPLA8 expression, indicating a null effect of his genetic variants (Supplementary Fig. 1C). Owing to the lack of patient-derived cells, we could not assess experimentally the splicing impact of c.2075-2A>G in Patient 2 and c.1684-2A>G in Patient 5. However, *in silico* analysis with SpliceAI[56] predicted that

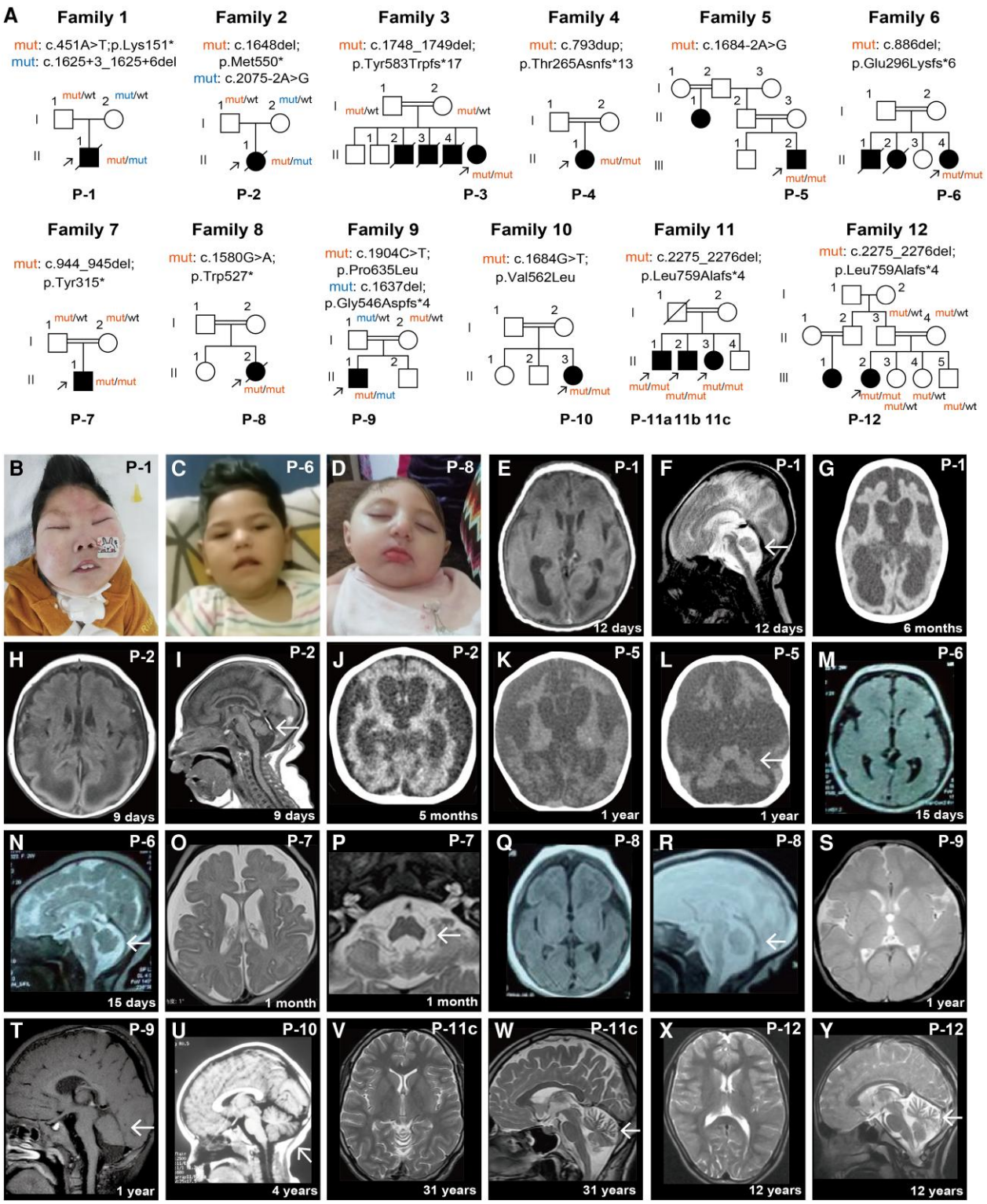

Figure 1 Identification of biallelic loss-of-function variants in *PNPLA8* in patients with diverse neurological phenotypes. (**A**) Pedigrees, showing autosomal recessive inheritance with biallelic *PNPLA8* variants in 12 unrelated families. The probands are indicated by arrows. Filled symbols denote affected individuals; squares represent males and circles females. Double lines indicate first-cousin status. Pathogenic or likely pathogenic variants in *PNPLA8* are denoted as 'mut', and WT sequences in *PNPLA8* are represented as 'wt'. (**B**–**D**) Clinical photographs of Patients 1, 6 and 8. (**E**–**G**) Axial T_1-weighted (**E**) and sagittal T_2-weighted (**F**) MRI images and a brain CT image (**G**) of Patient 1. The arrow indicates pontocerebellar hypoplasia. (**H**–**J**) T_1-weighted images of MRI (**H** and **I**) and a brain CT image (**J**) of Patient 2. The arrow indicates pontocerebellar hypoplasia. (**K** and **L**) Brain CT images of Patient 5. The arrow indicates cerebellar atrophy. (**M** and **N**) Axial T_1-weighted (**M**) and sagittal T_2-weighted (**N**) MRI images of Patient 6. The arrow indicates pontocerebellar hypoplasia. (**O** and **P**) T_2-weighted MRI images of Patient 7. The arrow indicates pontocerebellar hypoplasia. (**Q** and **R**) Axial T_1-weighted (**Q**) and sagittal T_2-weighted (**R**) MRI images of Patient 8. The arrow indicates pontocerebellar hypoplasia. (**S** and **T**) Axial T_2-weighted (**S**) and sagittal T_1-weighted (**T**) MRI images of Patient 9. The arrow indicates cerebellar atrophy. (**U**) T_1-weighted MRI images of Patient 10, with very mild cerebellar atrophy (arrow). (**V** and **W**) T_2-weighted MRI images of Patient 11c, exhibiting cerebellar atrophy (arrow). (**X** and **Y**) T_2-weighted MRI images of Patient 12, exhibiting cerebellar atrophy (arrow). Each patient is labelled as P-1 (Patient 1), P-2 (Patient 2), etc.

c.2075-2A>G and c.1684-2A>G result in the loss of a splice acceptor site with a Δ score of 0.97 and 0.93, respectively (high-specificity cut-off: 0.8). Collectively, 12 of 14 individuals carried the combination of nonsense, frameshift and splice-site variants, which suggests LoF in PNPLA8.

Clinical spectrum of *PNPLA8*-related neurological disease

We collected clinical information from the newly identified patients (Table 1; facial photographs in Fig. 1B–D; additional details in Supplementary Table 1; case reports in the Supplementary material). Highly frequent clinical features of our patients were central hypotonia (100%, 13/13), dystonia (67%, 8/12), seizure (71%, 10/14) and cerebellar atrophy (100%, 12/12). Among the 14 patients, eight patients (Families 1–8; Fig. 1B–D) were characterized further by several common features, such as congenital microcephaly (71%, 5/7), global developmental delay attaining no milestones (100%, 7/7), peripheral spasticity (88%, 7/8) and early-onset seizure within 7 months of age (100%, 8/8). Neuroimaging revealed that these patients showed a simplified gyral pattern (100%, 6/6), pontocerebellar hypoplasia (100%, 7/7) and severe progressive atrophy of the cerebral cortex (100%, 5/5; Fig. 1E–R). In contrast, four patients (Families 11–12) were characterized by relatively mild features: attaining the milestone of walking (100%, 4/4), ataxia (75%, 3/4), regression of milestones (100%, 4/4), mild or no intellectual disability (75%, 3/4) and unique or absent seizures (100%, 4/4). Brain MRI showed little or no cerebral cortical volume loss but progressive cerebellar atrophy, consistent with the pronounced movement disorder observed in patients (100%, 3/3; Fig. 1V–Y and Supplementary Videos 1 and 2). The remaining patient (Families 9 and 10) showed intermediate severity. Brain MRI also showed cerebellar atrophy (Fig. 1S–U).

We next assessed the correlation between the phenotypic features and the corresponding *PNPLA8* variants. By combining previously reported 11 affected individuals from eight families, we performed intergroup comparisons (Table 1, Fig. 2 and Supplementary Table 1). Eight patients (Families 1–8) and seven previously reported infants[23,25,27,29] were at the severe end of the spectrum (Table 1). Regarding their genotypes, biallelic LoF variants affecting three or four PNPLA8 protein isoforms were associated specifically with this group (Fig. 2). Two patients (Families 9 and 10) and two previously reported children[24,25] had intermediate severity (Table 1). These four patients carried the combination of either a LoF variant, missense variants or a recurrent frameshift variant (p.Leu759Alafs*4) located at the C-terminus (Fig. 2). Four patients (Families 11–12) and two previously reported adults[26] shared a relatively mild neurodegenerative phenotype characterized by late-onset movement disorders (Table 1 and Supplementary Table 1). All the patients in this group harboured biallelic C-terminal frameshift variants (p.Thr757Glnfs*10 or p.Leu759Alafs*4) (Fig. 2).

Surprisingly, we identified two additional individuals from two unrelated Iranian families with biallelic variants in *PNPLA8* from another non-neurological cohort (Families 13 and 14; Supplementary Fig. 2A and B and Supplementary Table 1). A patient from one family showed optic atrophy, and the other patient showed non-syndromic hearing loss. These patients were homozygous for distinct N-terminal frameshift variants, which affect only the largest protein isoform (molecular weight 88 kDa) owing to the multiple translation start sites in *PNPLA8*[11] (Fig. 2). It is worth noting that in the family showing optic atrophy, there was an affected sibling of the proband, while he was heterozygous for the variant (Supplementary Fig. 2B). These findings indicate the undetermined significance of these N-terminal frameshift variants, although biallelic LoF variants in *PNPLA8* have been linked to neurological diseases. Collectively, our data suggest that biallelic LoF variants affecting two protein isoforms (molecular weights 77 and 74 kDa) are sufficient for the severe developmental and progressive phenotype.

To evaluate the molecular effects of the identified variants, we tested PNPLA8 protein expression and the amounts of mitochondrial phospholipids using skin fibroblasts from patients. We found that the LoF variant identified in the severe case (Patient 6: p.Glu296Lysfs*6) resulted in a null effect, similar to Patient 1. In contrast, LoF variants identified in non-severe cases (Patient 12, mild phenotype with p.Leu759Alafs*4; Patient 14, non-neuronal phenotype with p.Val7*) exhibited weak expression of the 77-kDa PNPLA8 protein, suggesting residual protein function

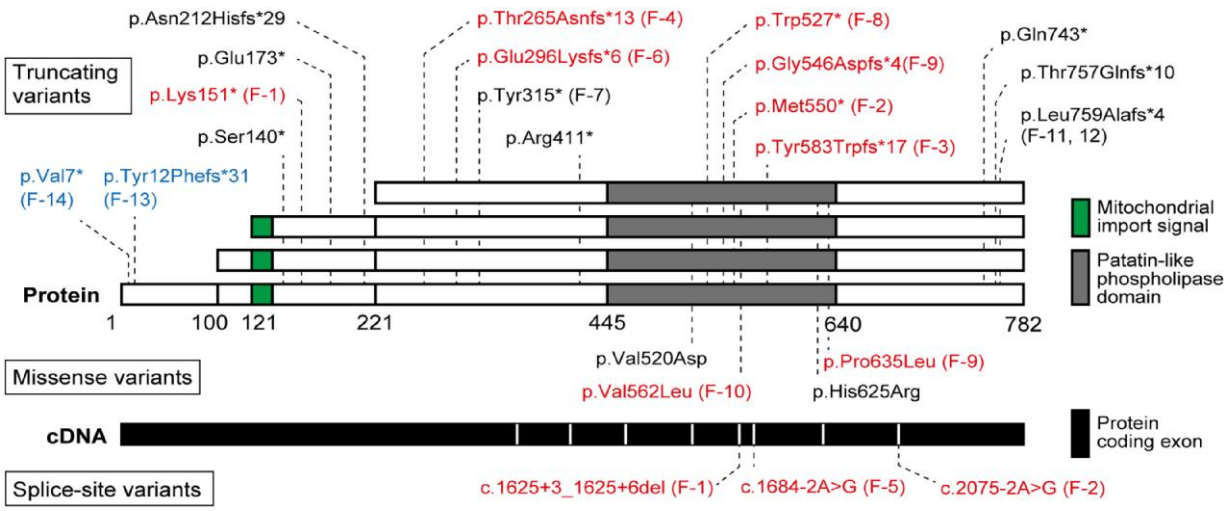

Figure 2 PNPLA8 protein isoforms, with the position of the identified variants. Schematic representation of PNPLA8 protein isoforms attributable to alternative translation initiation sites (*top*) and *PNPLA8* exon locations reflecting the canonical full-length transcript (NM_001256007.3, *bottom*). Novel disease-associated variants (*red*) and previously reported variants[23–29] (*black*) are noted. The variants identified from non-neuronal cohorts are noted in *blue*. Each family is labelled as F-1 (Family 1), F-2 (Family 2), etc.

(Supplementary Fig. 2C). In contrast, the missense variant identified in the previously reported patient[27] (severe phenotype with homozygous p.Val520Asp) resulted in a similar protein expression level to the controls despite the severe phenotype (Supplementary Fig. 2C). Given the localization of PNPLA8 on mitochondria,[12] we next analysed the abundance of mitochondrion-specific phospholipids, CL and monolysocardiolipin (MLCL).[57] Although a significant correlation was not observed between CL/MLCL abundance and phenotypic severity, the abundance of CL and MLCL appeared to be decreased in patient-derived skin fibroblasts compared with control samples (Supplementary Fig. 2D and E). Our findings suggest that variants in *PNPLA8* contribute to alterations in phospholipid metabolism.

Phenotypic characterization of *PNPLA8* KO cerebral organoids

From the genotype–phenotype analysis, we hypothesized that disrupted function of PNPLA8 leads to developmental encephalopathy and congenital microcephaly representing the severe end of the phenotypic spectrum. To test whether and how *PNPLA8* disruption affects the developing brain, we generated cerebral organoids using human iPSCs. We generated isogenic iPSC lines using single guide RNAs (sgRNAs), which were designed to disrupt all the protein isoforms by targeting the first two exons of *PNPLA8* (Fig. 3A). Using CRISPR/Cas9 genome-editing technology, the designed sgRNA and Cas9 protein were introduced into the previously established iPSC line.[35-37] We obtained two sets of iPSC clones with homozygous truncating variants in *PNPLA8* (Fig. 3B). We confirmed the efficient deletion of PNPLA8 protein by immunoblotting (Fig. 3C). We next generated cerebral organoids from *PNPLA8* KO iPSCs and control (WT) iPSCs[39,40,58,59] (Fig. 3D). The cerebral organoids continued to grow for ≤12 weeks, with the appearance of multiple ventricle-like structures (Fig. 3E). The organization of cortical structures, namely SOX2$^+$ ventricular zone-like regions (VZ) and TUJ1$^+$ neuronal areas around the VZ, was confirmed[58,60] (Supplementary Fig. 3A).

There was no difference in the organoid surface area between *PNPLA8* KO and WT cerebral organoids at 4 weeks of culture (Supplementary Fig. 3B). Given that the organoid surface area was not quantifiable after 4 weeks of culture owing to the cutting procedure (detailed in the 'Materials and methods' section), we next evaluated the expanding potential of the proliferative zones in the cerebral organoids. According to established terminology,[61] two proliferative zones were determined: the VZ composed of densely packed SOX2$^+$ aRGCs,[58-60] and the subventricular zone-like regions (SVZ), composed of sparsely distributed SOX2$^+$ NPCs and TBR2$^+$ bIPs[58-60] (Fig. 3F and G and Supplementary Fig. 3C). We found that the SVZ area was smaller in *PNPLA8* KO cerebral organoids compared with WT cerebral organoids at 12 weeks, whereas there was no significant difference at 8 weeks of culture (Fig. 3F and H). The size of the VZ area was similar between WT and *PNPLA8* KO cerebral organoids at both time points (Fig. 3F and I). The perimeter and thickness of the SVZ, but not the VZ, were also smaller in *PNPLA8* KO cerebral organoids than in WT cerebral organoids (Fig. 3F and Supplementary Fig. 3D–H). These data suggest that loss of PNPLA8 impairs the expansion of SVZ, but not VZ.

To investigate the neurogenic consequences of the reduced SVZ size in *PNPLA8* KO cerebral organoids, we quantified the number of neurons in the cortical plate-like region containing deep- and upper-layer neurons.[60] The number of SATB2$^+$ upper-layer neurons was significantly reduced in *PNPLA8* KO cerebral organoids compared with WT cerebral organoids (Fig. 3J and K and Supplementary Fig. 3I). In contrast, there was no significant difference in the number of CTIP2$^+$ deep-layer neurons (Fig. 3J and L). The decreased number of upper-layer neurons is in agreement with our findings of the reduced SVZ size in *PNPLA8* KO cerebral organoids and suggests a preferential reduction in the number of bRGCs in the SVZ, because bRGCs have been linked to the production of upper-layer neurons.[2,62,63]

Loss of PNPLA8 reduces the abundance of bRGCs in the SVZ

To investigate the cell types contributing to the reduced expansion of the SVZ in *PNPLA8* KO cerebral organoids, we quantified the number of bRGCs and bIPs in the SVZ at 12 weeks of culture. The number of PAX6$^+$HOPX$^+$ bRGCs in the SVZ was significantly reduced in *PNPLA8* KO cerebral organoids compared with WT cerebral organoids (Fig. 4A and B). In contrast, the number of TBR2$^+$ bIPs was similar between WT and *PNPLA8* KO cerebral organoids (Fig. 4C and D). These data suggest that the reduced abundance of bRGCs mainly contributes to the reduced size of SVZ in *PNPLA8* KO cerebral organoids.

To investigate how the number of bRGCs was reduced in *PNPLA8* KO cerebral organoids, we first quantified the number of mitotic cells in the cerebral organoids at 12 weeks of culture. The number of phospho-H3$^+$ mitotic cells at the apical surface, where aRGCs divide,[64] was similar between *PNPLA8* KO cerebral organoids and WT cerebral organoids (Supplementary Fig. 4A and B). The number of phospho-H3$^+$SOX2$^+$ NPCs in the SVZ was also similar between *PNPLA8* KO cerebral organoids and WT cerebral organoids (Supplementary Fig. 4A and C). We next quantified the number of apoptotic cells in the cerebral organoids at 12 weeks of culture. The number of cleaved Caspase 3$^+$ apoptotic cells in the VZ and SVZ was similar between *PNPLA8* KO cerebral organoids and WT cerebral organoids (Supplementary Fig. 4D–F). To assess cell division, BrdU was introduced into the culture medium for a 24-h period to label cells in the S phase, then cerebral organoids were fixed for immunostaining with PCNA, Ki67 and BrdU (Fig. 4E). No differences were detected in the numbers of either Ki67$^+$ or PCNA$^+$ cells in the VZ, suggesting that the number of cycling cells was not altered in *PNPLA8* KO cerebral organoids (Fig. 4F and G and Supplementary Fig. 4G and H). Interestingly, the number of BrdU$^+$ cells was increased in *PNPLA8* KO cerebral organoids compared with WT cerebral organoids (Fig. 4F and H). Collectively, our results suggest that the length of the S phase was altered in the VZ of *PNPLA8* KO cerebral organoids, potentially leading to a decreased production rate of bRGCs and neurons in a given time frame.

Patient-derived cerebral organoids phenocopy *PNPLA8* knockout cerebral organoids

Analysis of *PNPLA8* KO cerebral organoids suggested a crucial role for *PNPLA8* in human brain development. However, it remained to be determined whether the *PNPLA8* variants found in patients have the same impact on neurogenesis. We next generated iPSCs by reprogramming peripheral blood monocytes derived from Patient 1 and his father (Control), because Patient 1 skin fibroblasts showed a significant reduction in PNPLA8 protein expression (Fig. 5A). Typical iPSC morphology and capacity to differentiate into three germ layers *in vitro* were confirmed for quality assurance[65] (Supplementary Fig. 5A and B). These iPSCs carried the same variants in *PNPLA8* as the patient from whom they were derived

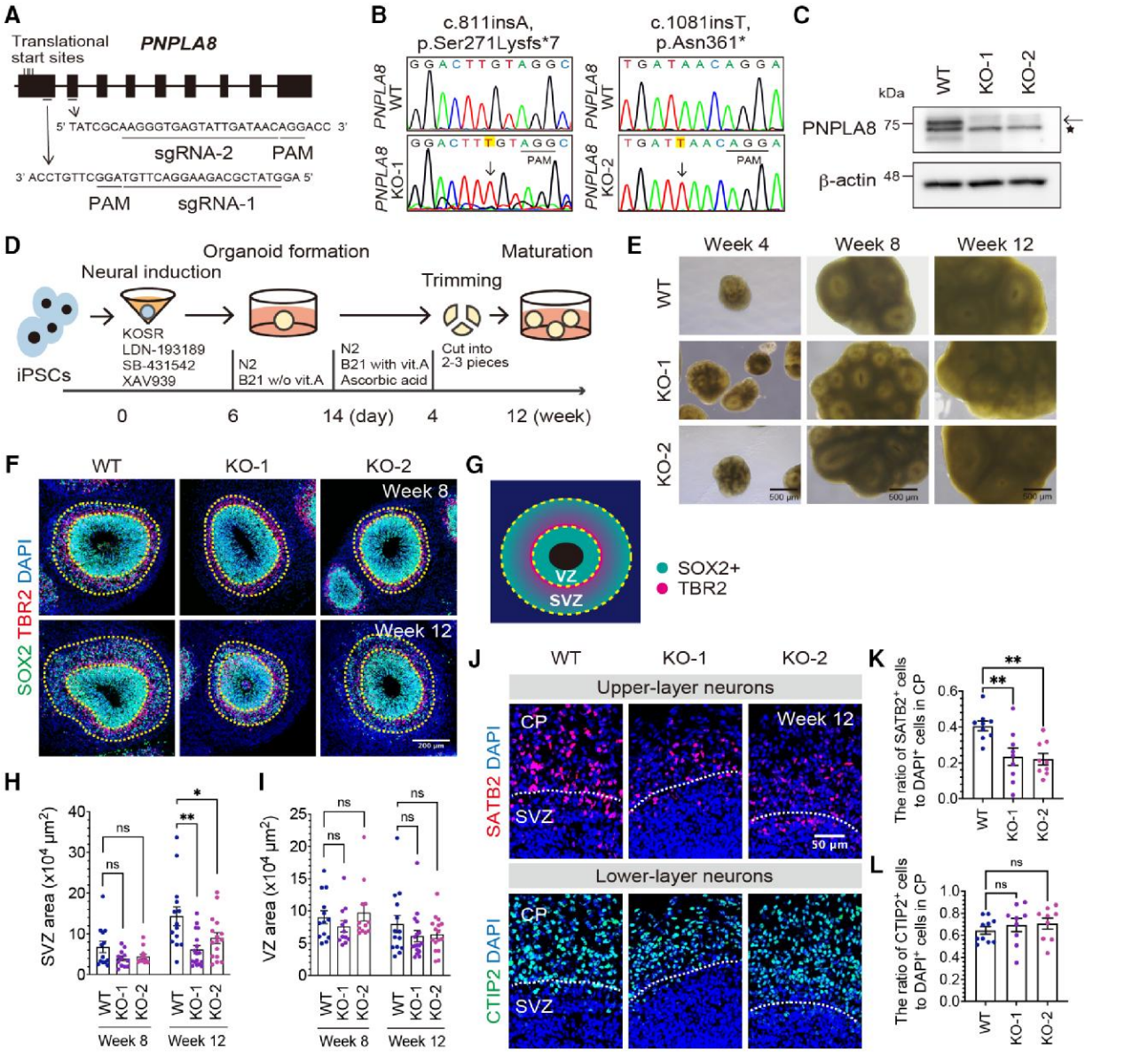

Figure 3 Loss of PNPLA8 reduces the size of subventricular zone-like regions and the number of upper-layer neurons in induced pluripotent stem cell-derived cerebral organoids. (**A**) Schematic representation of the designed sequence of single guide RNA (sgRNA) next to protospacer adjacent motif (PAM) for *PNPLA8*. (**B**) Sanger sequencing of the CRISPR/Cas9-mediated homozygous nucleotide insertion in induced pluripotent stem cell (iPSC) lines. Altered sequences are indicated by an arrow and are highlighted in yellow. (**C**) Immunoblotting analysis of PNPLA8 using wild-type (WT) and *PNPLA8* knockout (KO) iPSC lines. β-Actin was used as an internal protein-loading control. The arrow indicates the estimated 77 kDa PNPLA8 band. The fold change of PNPLA8 levels relative to β-actin, as quantified from protein bands (WT, KO-1 and KO-2), was 1.05 ± 0.07, 0.07 ± 0.07 and 0.04 ± 0.01, respectively (WT versus KO-1, $P < 0.0001$; WT versus KO-2, $P < 0.0001$), based on data obtained from four independent technical experiments. The asterisk indicates a non-specific band. Full-length blots are shown in Supplementary Fig. 9C. (**D**) Schematic illustration of the generation of cerebral organoids from *PNPLA8* KO and WT iPSC lines. KOSR and B21 indicate knockout serum replacement and Brew 21, respectively. (**E**) Bright-field microscopy images of cerebral organoids at different developmental time points. Scale bars = 500 μm. (**F** and **G**) Representative immunofluorescence images of neural stem and progenitor cell (NPC) marker, SOX2, basal intermediate progenitor cell (bIP) marker, TBR2, and nuclear marker, DAPI, at 8 and 12 weeks of culture. ventricular zone-like regions (VZ) and subventricular zone-like regions (SVZ) are highlighted according to the spatial distribution of NPCs. Scale bars = 200 μm. (**H** and **I**) Quantification of the surface area of the VZ (**H**) and SVZ (**I**) at 8 and 12 weeks of culture. Average values ± SEM from the number of organoids in three independent experiments (at least three organoids per experiment) are plotted: WT at week 8 ($n = 13$); WT at week 12 ($n = 14$); KO-1 at week 8 ($n = 12$); KO-1 at week 12 ($n = 17$); KO-2 at week 8 ($n = 12$); KO-2 at week 12 ($n = 16$). *$P < 0.05$, **$P < 0.01$; ns = not significant. One-way ANOVA followed by Dunnett's multiple comparisons test for each time point. (**J**) Representative immunofluorescence images of CTIP2⁺ deep-layer neurons and SATB2⁺ upper-layer neurons at 12 weeks of culture. Scale bar = 50 μm. (**K** and **L**) Quantification of the SATB2⁺ cells (**K**) and CTIP2⁺ cells (**L**) in the cortical plate-like region (CP). Average values ± SEM from three independent experiments (at least three organoids per experiment) are plotted: WT ($n = 9$); KO-1 ($n = 9$); KO-2 ($n = 9$). **$P < 0.01$; ns = not significant. One-way ANOVA followed by Dunnett's multiple comparisons test.

(Supplementary Fig. 5C). Immunoblotting showed a significant reduction of PNPLA8 protein in Patient 1-derived iPSCs and *PNPLA8* KO iPSCs (Supplementary Fig. 5D). Patient 1-derived iPSCs were induced into cerebral organoids with a slightly different protocol from that for *PNPLA8* KO cerebral organoids by using Matrigel for more efficient induction (Supplementary Fig. 5E).[58,66,67] The cerebral organoids were cultured for 8 weeks before being evaluated (Fig. 5B). Patient 1-derived cerebral organoids showed a reduced SVZ size and

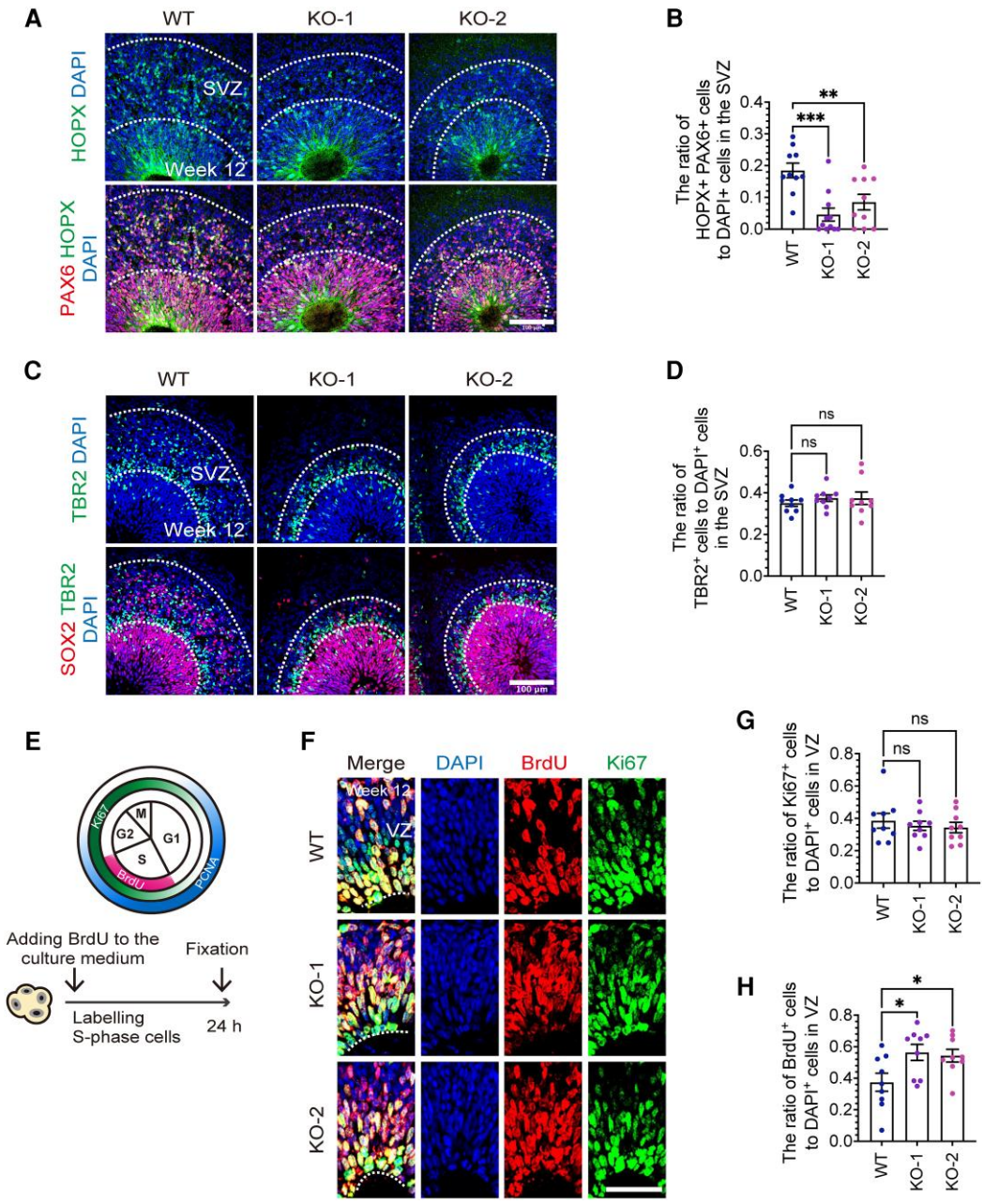

Figure 4 There is a reduced number of basal radial glial cells in the subventricular zone-like regions of *PNPLA8* knockout cerebral organoids. (**A**) Representative immunofluorescence images of PAX6$^+$HOPX$^+$ basal radial glial cells (bRGCs) at 12 weeks of culture. Scale bar = 100 µm. (**B**) Quantification of PAX6$^+$HOPX$^+$ bRGCs in a 100-µm-wide field of subventricular zone-like regions (SVZ). SVZ is highlighted according to the spatial distribution of neural stem and progenitor cells (NPCs). Average values ± SEM from three independent experiments (at least three organoids per experiment) are plotted: WT ($n = 10$); KO-1 ($n = 11$); KO-2 ($n = 10$). $^*P < 0.05$, $^{**}P < 0.01$, $^{***}P < 0.001$. One-way ANOVA followed by Dunnett's multiple comparisons test. (**C**) Representative immunofluorescence images of SOX2$^+$ NPCs and TBR2$^+$ basal intermediate progenitor cells (bIPs) at 12 weeks of culture. Scale bar = 100 µm. (**D**) Quantification of TBR2$^+$ bIPs in a 100-µm-wide field of SVZ. SVZ is highlighted according to the spatial distribution of NPCs. Average values ± SEM from three independent experiments (three organoids per experiment) are plotted: WT ($n = 9$); KO-1 ($n = 9$); KO-2 ($n = 9$). ns = not significant. One-way ANOVA followed by Dunnett's multiple comparisons test. (**E**) Schematic illustrations of the labelling protocols for estimation of the cell cycle. Cerebral organoids were treated with bromodeoxyuridine (BrdU) for 24 h to identify cells undergoing the S phase. (**F**) Representative immunofluorescence images of BrdU$^+$ cells and Ki67$^+$ cells at 12 weeks of culture. Scale bar = 50 µm. (**G** and **H**) Quantification of Ki67$^+$ cells (**G**) and BrdU$^+$ cells (**H**) in the VZ. Average values ± SEM from three independent experiments (three organoids per experiment) are plotted: WT ($n = 9$); KO-1 ($n = 9$); KO-2 ($n = 9$). $^{**}P < 0.01$; ns = not significant. One-way ANOVA followed by Dunnett's multiple comparisons test.

a slightly increased VZ size compared with Control cerebral organoids (Supplementary Fig. 5F–H).

Patient 1-derived cerebral organoids exhibited a reduced number of PAX6$^+$HOPX$^+$ bRGCs in the SVZ compared with Control cerebral organoids at 8 weeks of culture (Fig. 5C and D). We also found that the number of HOPX$^+$ cells in the VZ was also reduced in Patient 1-derived cerebral organoids (Fig. 5E and F). In contrast, the number of TBR2$^+$ bIPs in the SVZ was similar between Patient 1-derived and Control cerebral organoids at 8 weeks of culture (Fig. 5G and H). The number of SATB2$^+$ upper-layer neurons was

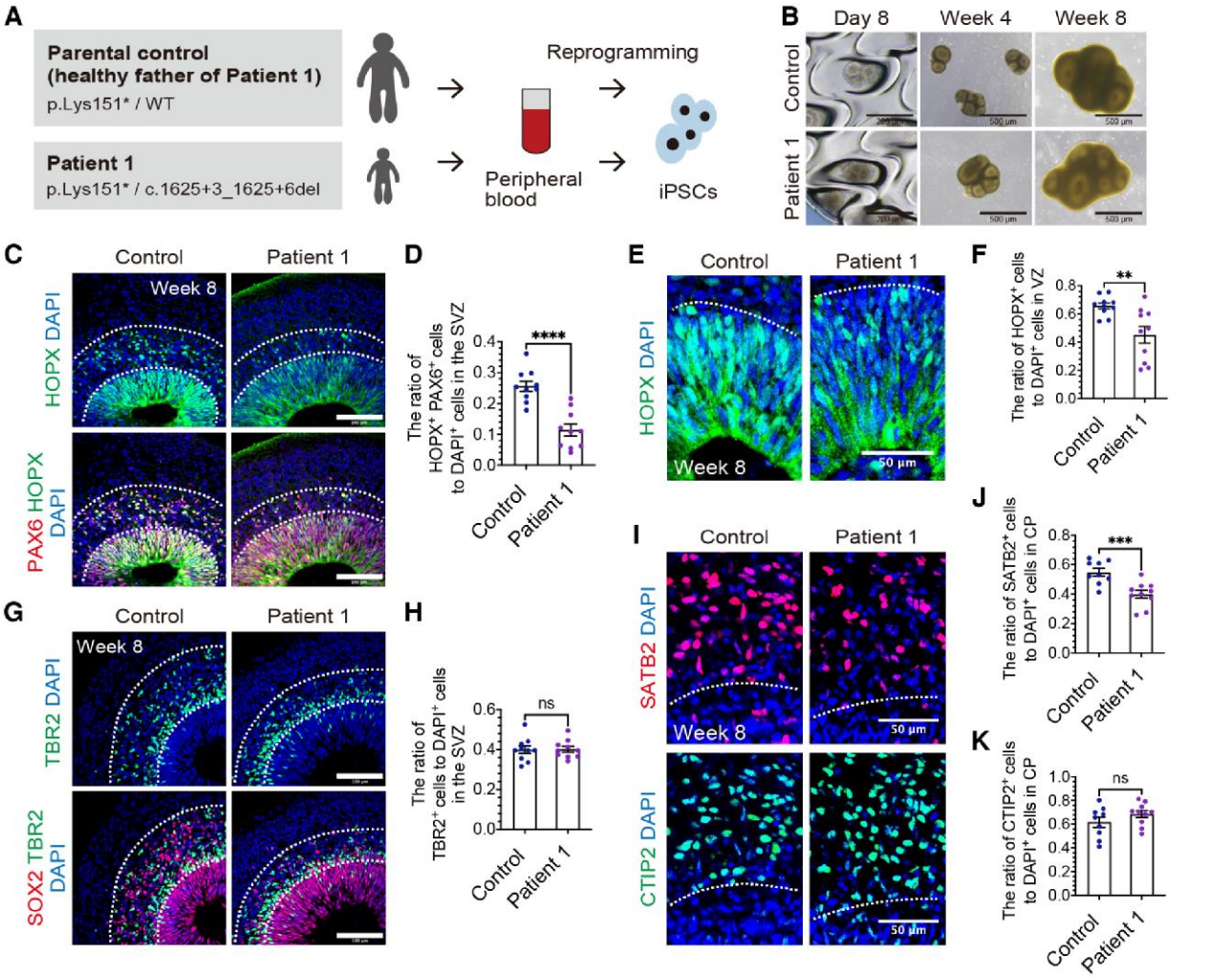

Figure 5 A reduced number of basal radial glial cells and upper-layer neurons in Patient 1 induced pluripotent stem cell-derived cerebral organoids. (**A**) Schematic view of generating induced pluripotent stem cells (iPSCs) from peripheral blood from Patient 1 and a parental control. (**B**) Bright-field microscopy images of cerebral organoids at different developmental time points. Scale bars = 500 μm. (**C** and **G**) Representative immunofluorescence images of basal radial glial cells (bRGCs) (**C**) and basal intermediate progenitor cells (bIPs) (**G**) at 8 weeks of culture. Scale bars = 100 μm. (**D** and **H**) Quantification of bRGCs (**D**) and bIPs (**H**) in a 100-μm wide field of subventricular zone-like regions (SVZ). The SVZ is highlighted according to the spatial distribution of neural progenitor cells. Average values ± SEM from three independent experiments (at least three organoids per experiment) are plotted: bRGCs of Patient 1 ($n = 10$); bRGCs of control ($n = 10$); bIPs of Patient 1 ($n = 10$); bIPs of control ($n = 10$). ****$P < 0.0001$; ns = not significant. Student's unpaired *t*-test with Welch's correction. (**E**) Representative immunofluorescence images of HOPX$^+$ cells in the ventricular zone-like region (VZ) at 8 weeks of culture. Scale bar = 50 μm. (**F**) Quantification of HOPX$^+$ cells in the VZ. Average values ± SEM from three independent experiments (at least three organoids per experiment) are plotted. Control ($n = 10$); Patient 1 ($n = 10$); **$P < 0.01$. Student's unpaired *t*-test with Welch's correction. (**I**) Representative immunofluorescence images of CTIP2$^+$ deep-layer neurons and SATB2$^+$ upper-layer neurons at 8 weeks of culture. Scale bars = 50 μm. (**J** and **K**) Quantification of the proportion of SATB2$^+$ (**J**) and CTIP2$^+$ (**K**) cells in the cortical plate-like region (CP). Average values ± SEM from three independent experiments (at least three organoids per experiment) are plotted: Control ($n = 9$); Patient 1 ($n = 10$); ***$P < 0.001$; ns = not significant. Student's unpaired *t*-test with Welch's correction.

significantly reduced in Patient 1-derived cerebral organoids compared with Control cerebral organoids, but there was no significant difference in the number of CTIP2$^+$ deep-layer neurons (Fig. 5I–K). These results confirmed not only the LoF nature of the *PNPLA8* variants identified in the patient, but also the phenotypic reproducibility of the cerebral organoid models derived from multiple iPS cell lines.

Loss of PNPLA8 impairs mitochondrial function in skin fibroblasts but not in NPCs

In previous studies on mice and human patients lacking PNPLA8 function, impairment of mitochondrial function and morphology was observed in affected organs.[15,17,24] To test whether loss of PNPLA8 affects mitochondria in an affected patient, we examined mitochondrial function and morphology in skin fibroblasts from Patient 1 (Supplementary Fig. 6A). Transmission electron microscopy analysis did not reveal altered mitochondrial morphology in the patient-derived skin fibroblasts (Supplementary Fig. 6B). However, live-cell assessment of mitochondrial OXPHOS activity using an extracellular flux analyser revealed that the maximal respiration level was significantly lower in the patient-derived skin fibroblasts than those from healthy controls (Supplementary Fig. 6C and D).

Given that the function and morphology of mitochondria are involved in the fate specification of aRGCs,[68] we hypothesized

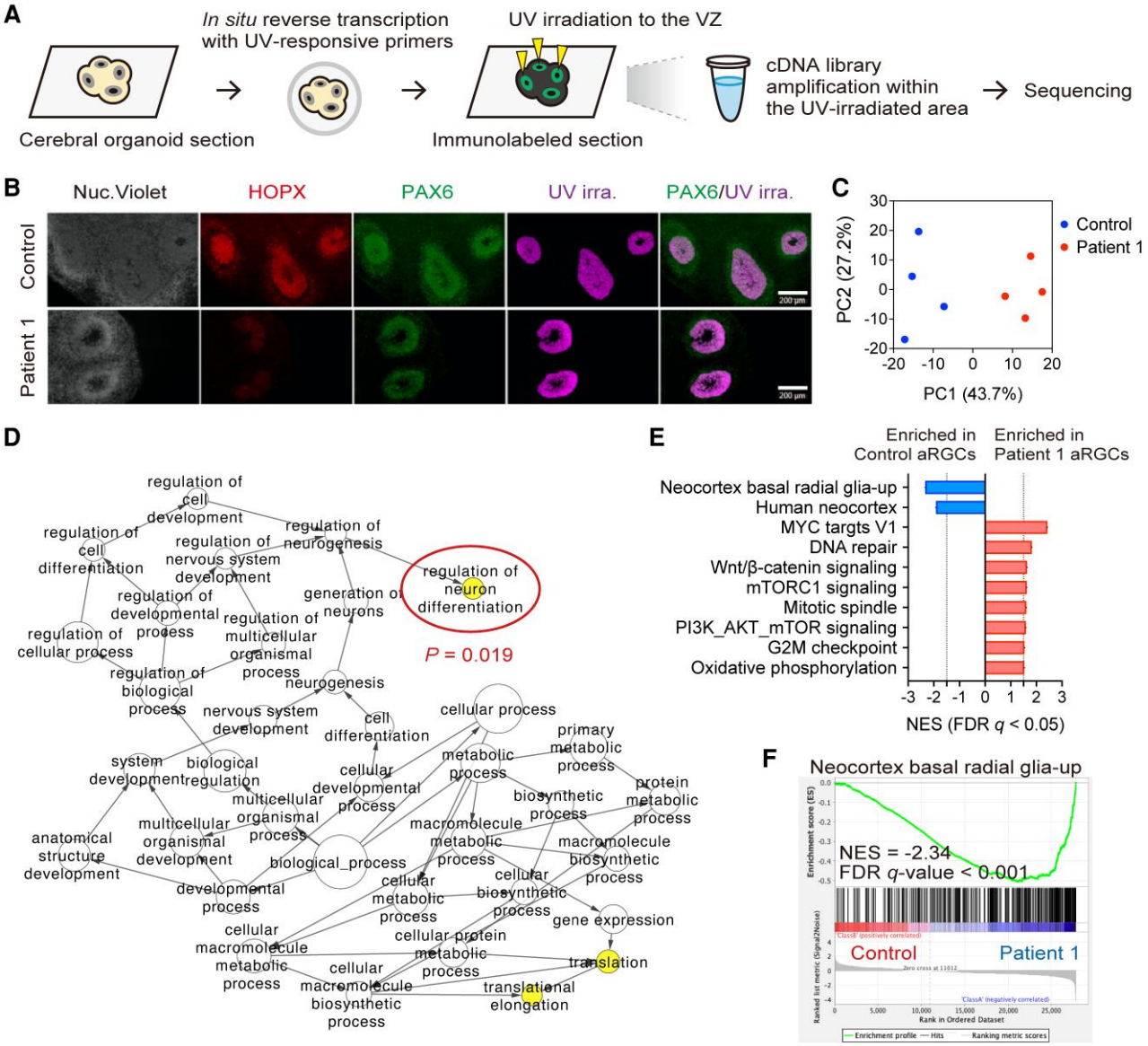

Figure 6 Spatially resolved differential gene expression profiles in the ventricular zone-like region of cerebral organoids. (**A**) Schematic overview of spatial transcriptomic analysis using the photo-isolation chemistry technique. (**B**) Representative immunofluorescence images of cerebral organoids at 8 weeks of culture. The ventricular zone-like region (VZ) and subventricular zone-like regions (SVZ) are visualized with PAX6 and HOPX. The VZ was irradiated with ultraviolet (UV) light where PAX6^{+} radial glial cells were densely packed. Merged images of immunofluorescence and the UV-irradiated area are shown (*right-most panels*). We extracted RNA samples from four distinct lines of cerebral organoids ($n = 4$). Each RNA sample was extracted from at least four VZs from at least two organoids. (**C**) Principal component analysis for the expression profiles. Principal component (PC)1 explained 43.7% and PC2 explained 27.2% of the variation. (**D**) Gene Ontology (GO)-term networks generated by BiNGO enrichment analysis for differentially expressed genes of patient apical radial glial cells. Node size represents the GO hierarchy. Yellow nodes indicate significant enrichment levels with $P < 0.05$. (**E**) Gene set enrichment analysis results ranked by normalized enrichment score (NES) using Curated gene sets and Hallmark gene sets of MSigDB signatures. Negative NES, depleted signature in Patient 1; positive NES, enriched signature in Patient 1. NES cut-off >1.5 or <−1.5. False-discovery rate *q*-value cut-off <0.05. (**F**) Enrichment plot for 'Neocortex basal radial glia-up', showing the profile of the running enrichment score and positions of gene set members on the rank-ordered list.

that mitochondrial function is impaired in *PNPLA8*-deficient aRGCs, which might alter determination of their fate, leading to the reduced production of bRGCs. To test this, we next generated adherent monolayer cultures of *PNPLA8* KO NPCs from the same iPSC lines we used for the cerebral organoid experiments and investigated mitochondrial morphology and function (Supplementary Fig. 6E). The generated cells expressed molecular markers of NPCs and formed rosette-like structures typical for a monolayer culture of NPCs[69,70] (Supplementary Fig. 6F). These cells were used as an alternative *in vitro* model to aRGCs. There were no dysmorphic mitochondria in *PNPLA8* KO NPCs, similar to the patient-derived skin fibroblasts (Supplementary Fig. 6G). Furthermore, live-cell assessment of cellular bioenergetics revealed that mitochondrial OXPHOS activity was also barely affected in *PNPLA8* KO NPCs (Supplementary Fig. 6H and I). These results suggest that mitochondria-related fate specification process is unlikely to be dysregulated in *PNPLA8*-deficient NPCs.

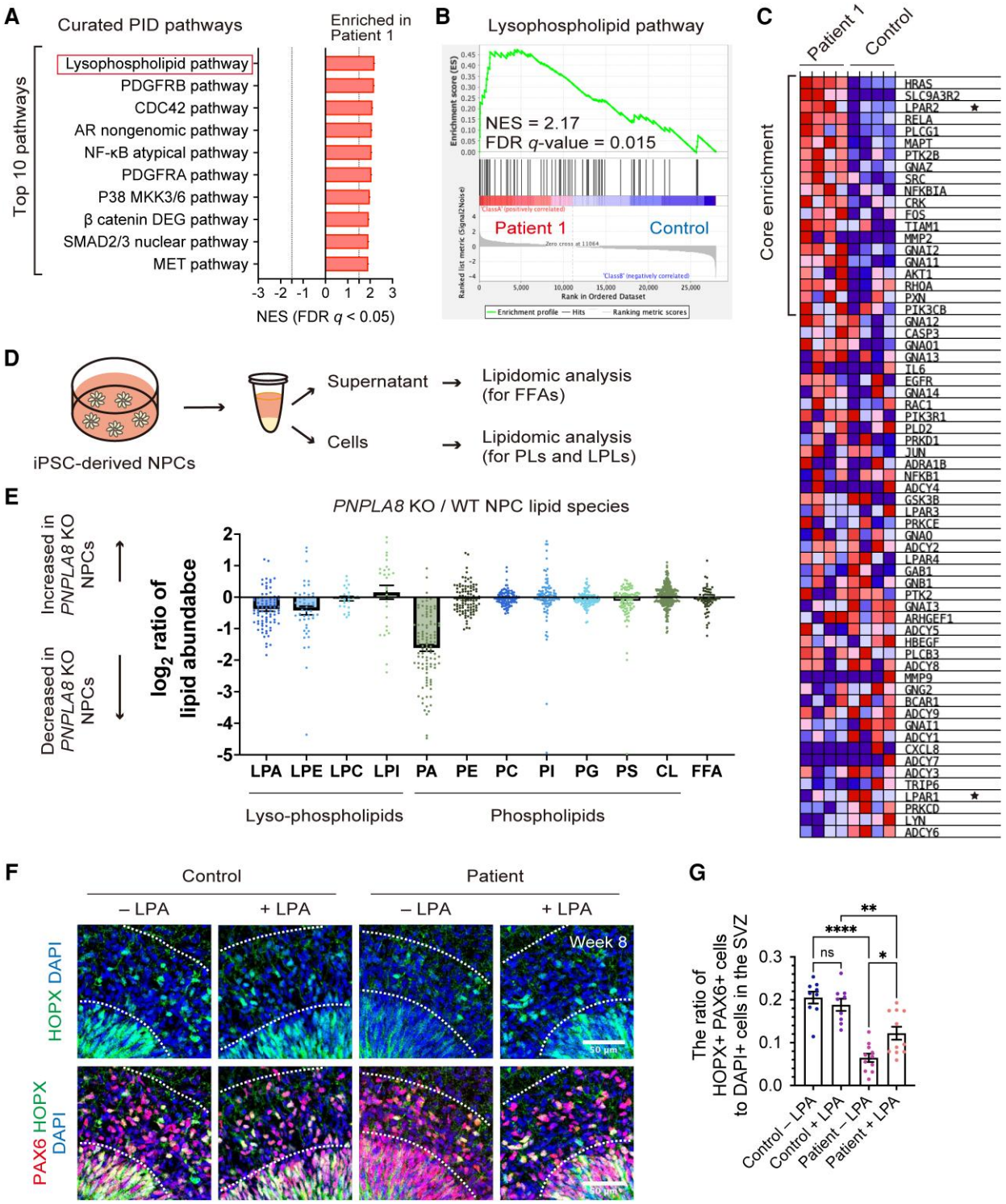

Figure 7 Loss of PNPLA8 affects phospholipid metabolism in neural progenitor cells, leading to reduced abundance of basal radial glial cells. (**A**) Gene set enrichment analysis results in the ventricular zone-like region (VZ) ranked by normalized enrichment score (NES) using the Pathway Interaction Database gene sets of MSigDB signatures. Positive NES, enriched signature in Patient 1. NES cut-off >1.5. False-discovery rate *q*-value cut-off <0.05. (**B**) Enrichment plot showing 'lysophospholipid pathway'. (**C**) Heat map of the marker genes from the 'lysophospholipid pathway' gene set in the comparison of Patient 1 apical radial glial cells (aRGCs; *left columns*) versus control aRGCs (*right columns*). Expression values are represented as colours and range from red (highest expression) to pink (moderate), light blue (low) and dark blue (lowest expression). The core enrichment genes, which contribute most to the enrichment result of the gene set, were determined by the running enrichment scores. (**D**) Induced pluripotent stem cell-derived neural progenitor cells (NPCs) and culture supernatants were subjected to lipidomic analysis to quantify phospholipids (PLs), lysophospholipids (LPLs) and free fatty acids (FFAs). (**E**) Individual lipid species detected in lipid extracts from wild-type (WT) NPCs or *PNPLA8* knockout (KO) NPCs, grouped by class. The $\log_2$ fold change values of liquid chromatography–mass spectrometry/mass spectrometry profiles are shown. Data from *PNPLA8* KO-1 and KO-2 NPCs are

(Continued)

Neurogenic gene expression is altered in aRGCs of patient-derived cerebral organoids

To explore further how corticogenesis is impaired in *PNPLA8*-deficient patients, we next performed spatial transcriptomics to assess spatially resolved gene expression levels in aRGCs of cerebral organoids generated from Patient 1-derived iPSCs. We used a photo-isolation chemistry technique that allowed us to determine expression profiles specifically from photo-irradiated ROIs.[42,43] According to the photo-isolation chemistry protocol, *in situ* reverse transcription was performed (Fig. 6A), and immunostaining defined the VZ (Fig. 6B). UV irradiation allowed for the VZ-specific amplification of cDNAs (Fig. 6A). The library preparation using the obtained cDNAs provided $>3.0 \times 10^6$ reads per sample. These reads were mapped to $>2.0 \times 10^4$ reference genes by RNA-seq analysis. Thus, we successfully obtained assessable spatial gene expression data from cerebral organoids. Principal component analysis showed distinct expression profiles between Control and Patient 1 samples (Fig. 6C).

To characterize gene expression profiles, we detected DEGs from the data. As shown in the heatmap of DEG clustering, there were 104 upregulated and 43 downregulated genes in Patient 1, compared with the Control (Supplementary Fig. 7A and Supplementary Table 3). The DEGs were analysed using Cytoscape-based BiNGO software for enrichment analysis.[44] Among three significantly enriched biological processes, we found the enrichment of 'regulation of neuron differentiation', suggesting a premature shift towards differentiating divisions in patient aRGCs (Fig. 6D). Next, we performed GSEA and determined significantly different expressions of gene sets from the mSigDB database.[46,47,71] Among the acquired data, we found that gene sets related to 'Neocortex basal radial glia-up' and 'Human neocortex' were much less enriched in Patient 1-derived cerebral organoids[45] (Fig. 6E and F). These results support our notion that loss of PNPLA8 impairs bRGC-mediated neurogenesis. We next created an enrichment map to visualize GSEA results using the GO tool as a gene-set source.[72] This visualization showed the enrichment of gene sets related to neuron development (e.g. 'regulation of axonogenesis') in Patient 1-derived cerebral organoids (Supplementary Fig. 7B). The GSEA results showed enrichment of multiple cell cycle-related gene sets, such as MYC targets, DNA repair, mitotic spindle and G2/M checkpoint, in Patient 1-derived cerebral organoids (Fig. 6E and Supplementary Fig. 7C).[73,74] The enrichment of WNT/β-catenin signalling mitochondrial OXPHOS, and mitochondrial organization was observed in Patient 1-derived cerebral organoids (Fig. 6E and Supplementary Fig. 7D). Collectively, our results suggest changes in the length of the cell cycle and potential dysregulation of the balance between progenitor pool expansion and neuronal differentiation.[68,75-78]

In addition, we investigated the differential gene expression profiles in the SVZ by spatial transcriptomics using Patient 1 and Control cerebral organoids (Supplementary Fig. 7E–G and Supplementary Table 4). GSEA revealed that the SVZ of Patient 1 cerebral organoids shared characteristic gene enrichment profiles observed in the VZ, such as bRGC, DNA repair, mTORC1 signalling, OXPHOS, G2/M checkpoint and MYC targets (Supplementary Fig. 7H).

Loss of PNPLA8 reduces the number of bRGCs through aberrant phospholipid metabolism

We next analysed pathways involved in the neurodevelopmental defects of *PNPLA8*-deficient patients using the transcriptomics data. The Pathway Interaction Database, a collection of curated pathways focusing on signalling and regulatory pathways rather than metabolic processes or generic mechanisms such as transcription and translation,[48] revealed 'lysophospholipid pathway' as the top-ranked enrichment only in the VZ of Patient 1-derived cerebral organoids (Fig. 7A and B and Supplementary Fig. 7I). Within the dataset, *LPAR2* was significantly enriched in Patient 1, whereas *LPAR1* was not enriched in Patient 1 (Fig. 7C). LPA acts as a signalling molecule through its distinct G protein-coupled receptors (LPAR1–6) with diverse effects during brain development.[79,80] Specifically, LPAR2 is thought to be involved in neural differentiation, whereas LPAR1 is likely to mediate various responses, such as proliferation.[80,81] These results suggest the possible link between dysregulated neurogenic signalling pathways and the aberrant phospholipid metabolism in *PNPLA8*-deficient aRGCs.

To examine whether loss of PNPLA8 affects phospholipid metabolism, we next performed lipidomic analysis using iPSC-derived NPCs and culture supernatants (Fig. 7D). The amounts of LPA, LPE and PA were decreased in *PNPLA8* KO NPCs compared with WT NPCs, whereas there was no significant difference in that of other phospholipids and free fatty acids (Fig. 7E). These results suggest that loss of PNPLA8 reduces the synthesis of LPA, LPE and PA through decreased PLA_2 activity. To examine a possible role of these phospholipids in the decrease in bRGC abundance, we subjected patient-derived cerebral organoids to a 7-day treatment in the presence or absence of LPA during the last week of culture. Treatment with LPA increased the number of bRGCs in Patient 1-derived cerebral organoids (Fig. 7F and G). These data suggest that PNPLA8-dependent phospholipid synthesis, or at least LPA, is crucial to ensure the abundance of bRGCs during human brain development.

Discussion

In this study, we provide insight into the understanding of *PNPLA8*-related neurological diseases (Supplementary Fig. 8). This insight is based on the clinical and genetic evaluation of newly identified patients with *PNPLA8* variants. Our data indicate that biallelic null variants in *PNPLA8* cause microcephaly through the reduced abundance of bRGCs. Our findings from the combination of iPSC-based models and multi-omics analysis suggest that PNPLA8 contributes to membrane remodelling and the fate-determination process in aRGCs.

Figure 7 Continued
combined as 'KO'. Bars represent the mean values for individual lipid species ± SEM for four independent experiments. Each dot indicates a single measurement of lysophosphatidic acid (LPA; $n = 83$), lysophosphatidylethanolamine (LPE; $n = 47$), lysophosphatidylcholine (LPC; $n = 24$), lysophosphatidylinositol (LPI; $n = 27$), phosphatidic acid (PA; $n = 104$), phosphatidylcholine (PC; $n = 104$), phosphatidylethanolamine (PE; $n = 101$), phosphatidylinositol (PI; $n = 92$), phoshatidylglycerol (PG; $n = 104$), phosphatidylserine (PS; $n = 89$), cardiolipin (CL; $n = 280$) and free fatty acids (FFA; $n = 64$). (**F**) Representative immunofluorescence images of $HOPX^+PAX6^+$ basal radial glial cells at 8 weeks of culture. Scale bars = 50 μm. (**G**) Quantification of the proportion of $HOPX^+PAX6^+$ cells in the subventricular zone-like region (SVZ). Average values ± SEM from three independent experiments (at least three organoids per experiment) are plotted: Control – LPA ($n = 9$); Control + LPA ($n = 9$); Patient–LPA ($n = 11$); Patient + LPA ($n = 11$); $^*P < 0.05$, $^{**}P < 0.01$, $^{****}P < 0.0001$; ns = not significant. One-way ANOVA followed by Dunnett's multiple comparisons test.

Our clinical data show the wide phenotypic spectrum of *PNPLA8*-related neurological diseases, forming a continuum ranging from mild to severe forms of developmental and degenerative epileptic–dyskinetic encephalopathy. Besides the phenotypic variability, our data allowed for the detailed evaluation of genotype–phenotype correlations. The homozygous recurrent C-terminal frameshift variants presented with a milder form of developmental and degenerative epileptic–dyskinetic encephalopathy, characterized by a late-onset movement disorder. According to the 'nonsense-mediated mRNA decay (NMD) rule', premature termination codons located 55 nucleotides or more downstream of the last exon–exon junction are considered to escape from NMD, leading to the translation of truncated protein.[82] As evidenced by Patient 12-derived cells exhibiting a detectable expression of PNPLA8 protein, the C-terminal truncating variant is likely to avoid NMD and lead to less severe clinical manifestations (Supplementary Fig. 2C).[26] In contrast, biallelic null variants affecting at least the 77 kDa protein isoforms presented with the severe form of developmental and degenerative epileptic–dyskinetic encephalopathy, characterized by early-onset severe neurological manifestations (Fig. 2). These patients typically showed congenital microcephaly and pontocerebellar hypoplasia. Termed as a novel clinical entity, 'pontocerebellar hypoplasia with microcephaly', the potential co-occurrence of these anomalies in cerebral and cerebellar structures has been proposed.[83] Our findings support this concept and imply a potential common mechanism underlying cortical and pontocerebellar development in humans.

Our CL/MLCL analysis using patient-derived skin fibroblasts did not reveal a clear correlation between the phenotype and mitochondrial phospholipid metabolism. It might come from the small number of patient samples or the tissue specificity, as indicated in previous research.[84] However, the usefulness of skin fibroblasts cannot be ruled out because a noticeable trend of reduction was observed in the comparison between patient samples and control samples regarding the amount of phospholipids. Further studies are needed to determine a biomarker that reflects the phenotypic severity.

The identification of our patients led to the initial hypothesis that complete loss of PNPLA8 function impairs corticogenesis. Using cerebral organoids lacking PNPLA8, we revealed a reduced abundance of bRGCs. A specific decrease in the number of upper-layer neurons supports the pathogenesis of microcephaly with the impairment of the expansion of bRGCs.[85] In this study, we used two slightly modified protocols for generating cerebral organoids from WT and *PNPLA8* KO samples, and from Control and Patient 1-derived samples. This was necessary because the initial method was inefficient for generating cerebral organoids using Control and Patient 1-derived iPSCs, primarily owing to the low formation rate of the VZ and SVZ. Given that our focus was to evaluate the number of bRGCs, we selected the evaluation time point based on the presence of bRGCs and the morphology of the VZ/SVZ. Despite the use of two slightly modified protocols, the impact of PNPLA8 on bRGCs was consistent. Given that *PNPLA8* variants can cause a broad spectrum of severity, further study is required to clarify the impact of the other variants, such as C-terminal truncating variant, on brain development.

Mitochondrial function has been linked to the fate decisions of NPCs.[68] However, loss of mitochondrial phospholipase PNPLA8 affected neither the function nor the morphology of mitochondria in NPCs, whereas there was a significant reduction of the maximum oxygen consumption in patient-derived skin fibroblasts. This discrepancy could be attributed to the energetic dependence, because NPCs are predominantly dependent on glycolytic metabolism rather than OXPHOS.[68] Given that neurons are dependent on OXPHOS,[68] mitochondrial dysfunction might also occur in neurons, thereby contributing to the progressive neurodegeneration of both the cerebrum and cerebellum. Our data indicate that loss of PNPLA8 appears to have little effect on NPC mitochondria and the fate-determining mechanisms in which mitochondria are involved.

By using a photo-isolation chemistry technique, we provide spatially resolved *in situ* transcriptional profiles of cerebral organoid sections. Our data indicate that aRGCs lacking PNPLA8 preferentially committed to differentiated neurons instead of bRGCs in cerebral organoids. The upregulation of gene sets related to 'DNA-repair' suggests an extended S phase in patient NPCs, because the S phase can be delayed in response to replication stress or diverse types of DNA damage.[86] Additionally, contrary to the fact that the transcriptional state of bRGC emerges in the VZ during early cortical neurogenesis,[87] the expression levels of bRGC-related genes were reduced in patient aRGCs. These data suggest that loss of PNPLA8 dysregulates the length of the cell cycle and reduces the production of bRGCs by altering the fate specification of aRGCs. The upregulation of lysophospholipid signalling genes in patient-derived cerebral organoids suggests the contribution of PNPLA8 to the fate-decision process with its membrane remodelling capacity. It needs to be addressed further whether PNPLA8-related phospholipid metabolism contributes to the fate-decision process and which pathway is involved in the pathogenesis through rescue experiments.

Our lipidomics data reveal the reduced abundance of LPA, LPE and PA in *PNPLA8* KO NPCs. In line with the unaffected morphology and function of mitochondria, the amount of CL was also unaffected in *PNPLA8* KO NPCs. The reduction of LPA and LPE can be explained by decreased PLA_2 activity.[88] However, the significant reduction of both LPA and PA suggests the impaired *de novo* synthesis of phospholipids.[89] Given that LPE can be catabolized to glycerol 3-phosphate, which is a starting material for the *de novo* synthesis of phospholipids, the reduction of LPE might also affect PA synthesis.[89] Collectively, it is likely that loss of PNPLA8 impairs phospholipid catabolism, leading to reduced synthesis of phospholipids in NPCs. The role of the PNPLA8-dependent phospholipid synthesis in bRGC genesis is supported further by our demonstration that the addition of LPA to the culture medium led to an increase in the number of bRGCs in patient-derived cerebral organoids. Pinson *et al.*[90] discussed how fatty acids are building blocks for membrane synthesis and are essential for bRGC proliferation in the developing modern human brain. It therefore appears worthwhile to investigate the relationship between PNPLA8-dependent phospholipid synthesis and human brain development.

Data availability

Sequencing data have been deposited in the National Center for Biotechnology Information Gene Expression Omnibus (GSE229956 and GSE248252).

Acknowledgements

Human iPSCs (Windy) were kindly provided by Dr Umezawa of the National Center for Child Health and Development (Tokyo, Japan). Fibroblast growth factor-2 was kindly provided by Dr Jeffrey L. Spees (University of Vermont, VT, USA). We thank Dr Padraig J. Flannery and Dr Nina Patel (Neurometabolic Unit, The National Hospital for Neurology and Neurosurgery, London, UK) for their

technical assistance in the mass spectrometry analysis. We are grateful for the technical assistance of the Research Equipment Sharing Center/Core Laboratory at Nagoya City University. We thank Dr Motoo Nakagawa, the neuroradiologist in Nagoya City University (Nagoya, Japan), for reviewing all the neuroimaging.

Funding

This study was supported by grants from the Japan Society for the Promotion of Science (grant numbers JP21463512, JP20K07907, JP21K07869, JP20K21584, JP21K07803, JP24K11048 and 24K02425) and the Japan Agency for Medical Research and Development (AMED; grant numbers JP24gm1210013, JP21wm0425007, JP20ek0109488, JP22ek0109486, JP22ek0109549 and JP22ek0109493). This study was also supported by grants from the Kawano Masanori Memorial Public Interest Incorporated Foundation for Promotion of Pediatrics and the Ono Medical Research Foundation to Y.N., the Daiko Foundation, The Hori Science and Arts Foundation, the Mochida Foundation for Medical and Pharmaceutical Research, the Takeda Science Foundation, iPS Academia Japan Inc., Leave a Nest Co. Ltd. (Ikeda Rika award) and a Grand-in-Aid for research in Nagoya City University (2013009) to I.S.S., and the Takeda Science Foundation to Y.K. H.S.D. is supported by the Cologne Clinician Scientist Program/Faculty of Medicine/University of Cologne and funded by the Deutsche Forschungsgemeinschaft (DFG, German Research Foundation, project no. 413543196) and by the Koeln Fortune Program/Faculty of Medicine, University of Cologne (project no. 371/2021, 243/2022). R.D.S.P. and M.F. are supported by a Medical Research Council (UK) Clinician Scientist Fellowship (MR/S002065/1) and a Medical Research Council (UK) award MC_PC_21046 to establish a National Mouse Genetics Network Mitochondria Cluster (MitoCluster). R.D.S.P. is supported by a Medical Research Council (UK) strategic award MR/S005021/1 to establish an International Centre for Genomic Medicine in Neuromuscular Diseases (ICGNMD), The Lily Foundation, Muscular Dystrophy UK (MDUK), the Rosetrees Trust and Stoneygate Foundation, and the LifeArc Centre to Treat Mitochondrial Diseases (LAC-TreatMito). MEXT Promotion of Development of a Joint Usage: The Cooperative Research Project Program, Medical Research Center Initiative for High Depth Omics, Coalition of Universities for Research Excellence Program (CURE) (JPMXP1323015486) and KAKENHI JP24H02323 (to Y.O.).

Competing interests

The authors report no competing interests.

Supplementary material

Supplementary material is available at *Brain* online.

References

1. Florio M, Huttner WB. Neural progenitors, neurogenesis and the evolution of the neocortex. *Development*. 2014;141:2182-2194.
2. Hansen DV, Lui JH, Parker PR, Kriegstein AR. Neurogenic radial glia in the outer subventricular zone of human neocortex. *Nature*. 2010;464:554-561.
3. Stepien BK, Vaid S, Huttner WB. Length of the neurogenic period—A key determinant for the generation of upper-layer neurons during neocortex development and evolution. *Front Cell Dev Biol*. 2021;9:676911.
4. Wang X, Tsai JW, LaMonica B, Kriegstein AR. A new subtype of progenitor cell in the mouse embryonic neocortex. *Nat Neurosci*. 2011;14:555-561.
5. Ostrem B, Di Lullo E, Kriegstein A. oRGs and mitotic somal translocation—A role in development and disease. *Curr Opin Neurobiol*. 2017;42:61-67.
6. Yu TW, Mochida GH, Tischfield DJ, et al. Mutations in *WDR62*, encoding a centrosome-associated protein, cause microcephaly with simplified gyri and abnormal cortical architecture. *Nat Genet*. 2010;42:1015-1020.
7. Zhang W, Yang SL, Yang M, et al. Modeling microcephaly with cerebral organoids reveals a WDR62-CEP170-KIF2A pathway promoting cilium disassembly in neural progenitors. *Nat Commun*. 2019;10:2612.
8. Mancuso DJ, Jenkins CM, Gross RW. The genomic organization, complete mRNA sequence, cloning, and expression of a novel human intracellular membrane-associated calcium-independent phospholipase A_2. *J Biol Chem*. 2000;275:9937-9945.
9. Tanaka H, Minakami R, Kanaya H, Sumimoto H. Catalytic residues of group VIB calcium-independent phospholipase A2 (iPLA2gamma). *Biochem Biophys Res Commun*. 2004;320:1284-1290.
10. Tanaka H, Takeya R, Sumimoto H. A novel intracellular membrane-bound calcium-independent phospholipase A2. *Biochem Biophys Res Commun*. 2000;272:320-326.
11. Murakami M, Masuda S, Ueda-Semmyo K, et al. Group VIB Ca^{2+}-independent phospholipase $A_2\gamma$ promotes cellular membrane hydrolysis and prostaglandin production in a manner distinct from other intracellular phospholipases A_2. *J Biol Chem*. 2005;280:14028-14041.
12. Mancuso DJ, Jenkins CM, Sims HF, Cohen JM, Yang J, Gross RW. Complex transcriptional and translational regulation of iPLA$_2\gamma$ resulting in multiple gene products containing dual competing sites for mitochondrial or peroxisomal localization. *Eur J Biochem*. 2004;271(23–24):4709-4724.
13. Hara S, Yoda E, Sasaki Y, Nakatani Y, Kuwata H. Calcium-independent phospholipase $A_2\gamma$ (iPLA$_2\gamma$) and its roles in cellular functions and diseases. *Biochim Biophys Acta Mol Cell Biol Lipids*. 2019;1864:861-868.
14. Mancuso DJ, Kotzbauer P, Wozniak DF, et al. Genetic ablation of calcium-independent phospholipase $A_2\gamma$ leads to alterations in hippocampal cardiolipin content and molecular species distribution, mitochondrial degeneration, autophagy, and cognitive dysfunction. *J Biol Chem*. 2009;284:35632-35644.
15. Mancuso DJ, Sims HF, Han X, et al. Genetic ablation of calcium-independent phospholipase $A_2\gamma$ leads to alterations in mitochondrial lipid metabolism and function resulting in a deficient mitochondrial bioenergetic phenotype. *J Biol Chem*. 2007;282:34611-34622.
16. Yoda E, Hachisu K, Taketomi Y, et al. Mitochondrial dysfunction and reduced prostaglandin synthesis in skeletal muscle of group VIB Ca^{2+}-independent phospholipase $A_2\gamma$-deficient mice. *J Lipid Res*. 2010;51:3003-3015.
17. Chao H, Liu Y, Fu X, et al. Lowered iPLA$_2\gamma$ activity causes increased mitochondrial lipid peroxidation and mitochondrial dysfunction in a rotenone-induced model of Parkinson's disease. *Exp Neurol*. 2018;300:74-86.
18. Eaddy AC, Cummings BS, McHowat J, Schnellmann RG. The role of endoplasmic reticulum Ca^{2+}-independent phospholipase $A_2\gamma$ in oxidant-induced lipid peroxidation, Ca^{2+} release, and renal cell death. *Toxicol Sci*. 2012;128:544-552.
19. Liu GY, Moon SH, Jenkins CM, et al. The phospholipase iPLA$_2\gamma$ is a major mediator releasing oxidized aliphatic chains from cardiolipin, integrating mitochondrial bioenergetics and signaling. *J Biol Chem*. 2017;292:10672-10684.

20. Sharma J, Eickhoff CS, Hoft DF, Ford DA, Gross RW, McHowat J. The absence of myocardial calcium-independent phospholipase $A_2\gamma$ results in impaired prostaglandin E_2 production and decreased survival in mice with acute *Trypanosoma cruzi* infection. *Infect Immun*. 2013;81:2278-2287.
21. Sharma J, McHowat J. PGE_2 release from tryptase-stimulated rabbit ventricular myocytes is mediated by calcium-independent phospholipase $A_2\gamma$. *Lipids*. 2011;46:391-397.
22. Harmouch F, Chahine N, Shbaro R, Alam CA. PNPLA 8 mutation in mitochondrial disease: Second case worldwide. *Acta Scientific Clinical Case Reports*. 2020;1:19-21.
23. Masih S, Moirangthem A, Phadke SR. Homozygous missense variation in *PNPLA8* causes prenatal-onset severe neurodegeneration. *Mol Syndromol*. 2021;12:174-178.
24. Saunders CJ, Moon SH, Liu X, et al. Loss of function variants in human *PNPLA8* encoding calcium-independent phospholipase $A_2\gamma$ recapitulate the mitochondriopathy of the homologous null mouse. *Hum Mutat*. 2015;36:301-306.
25. Shukla A, Saneto RP, Hebbar M, Mirzaa G, Girisha KM. A neurodegenerative mitochondrial disease phenotype due to biallelic loss-of-function variants in *PNPLA8* encoding calcium-independent phospholipase A2γ. *Am J Med Genet A*. 2018;176:1232-1237.
26. Burnyte B, Vilimiene R, Grigalioniene K, Adomaitiene I, Utkus A. Cerebellar ataxia and peripheral neuropathy in a family with *PNPLA8*-associated disease. *Neurol Genet*. 2023;9:e200068.
27. Abdel-Hamid MS, Abdel-Salam GMH, Abdel-Ghafar SF, Zaki MS. Delineating the phenotype of *PNPLA8*-related mitochondriopathies. *Clin Genet*. 2024;105:92-98.
28. Denomme-Pichon AS, Vitobello A, Olaso R, et al. Accelerated genome sequencing with controlled costs for infants in intensive care units: A feasibility study in a French hospital network. *Eur J Hum Genet*. 2022;30:567-576.
29. Fields C, Yozawitz E, Breilyn M, et al. Variants in PNPLA8 are associated with developmental epileptic encephalopathy and cerebellar atrophy. *Neurology*. 2022;98(suppl 18):P6-5.002.
30. Chou JH, Roumiantsev S, Singh R. PediTools electronic growth chart calculators: Applications in clinical care, research, and quality improvement. *J Med Internet Res*. 2020;22:e16204.
31. Kuczmarski RJ, Ogden CL, Guo SS, et al. CDC growth charts for the United States: Methods and development. *Vital Health Stat 11*. 2002;246:1-190.
32. Efthymiou S, Salpietro V, Malintan N, et al. Biallelic mutations in neurofascin cause neurodevelopmental impairment and peripheral demyelination. *Brain*. 2019;142:2948-2964.
33. Kato K, Miya F, Hamada N, et al. *MYCN* de novo gain-of-function mutation in a patient with a novel megalencephaly syndrome. *J Med Genet*. 2019;56:388-395.
34. Saida K, Maroofian R, Sengoku T, et al. Brain monoamine vesicular transport disease caused by homozygous *SLC18A2* variants: A study in 42 affected individuals. *Genet Med*. 2023;25:90-102.
35. Nishino K, Toyoda M, Yamazaki-Inoue M, et al. Defining hypomethylated regions of stem cell-specific promoters in human iPS cells derived from extra-embryonic amnions and lung fibroblasts. *PLoS One*. 2010;5:e13017.
36. Iwao T, Toyota M, Miyagawa Y, et al. Differentiation of human induced pluripotent stem cells into functional enterocyte-like cells using a simple method. *Drug Metab Pharmacokinet*. 2014;29:44-51.
37. Kondo Y, Iwao T, Yoshihashi S, et al. Histone deacetylase inhibitor valproic acid promotes the differentiation of human induced pluripotent stem cells into hepatocyte-like cells. *PLoS One*. 2014;9:e104010.
38. Schuster S, Saravanakumar S, Schöls L, Hauser S. Generation of a homozygous CRISPR/Cas9-mediated knockout human iPSC line for the *STUB1* locus. *Stem Cell Res*. 2019;34:101378.
39. Sloan SA, Andersen J, Pasca AM, Birey F, Pasca SP. Generation and assembly of human brain region-specific three-dimensional cultures. *Nat Protoc*. 2018;13:2062-2085.
40. Xiang Y, Tanaka Y, Cakir B, et al. hESC-derived thalamic organoids form reciprocal projections when fused with cortical organoids. *Cell Stem Cell*. 2019;24:487-497.e7.
41. Sakaguchi H, Kadoshima T, Soen M, et al. Generation of functional hippocampal neurons from self-organizing human embryonic stem cell-derived dorsomedial telencephalic tissue. *Nat Commun*. 2015;6:8896.
42. Honda M, Kimura R, Harada A, et al. Photo-isolation chemistry for high-resolution and deep spatial transcriptome with mouse tissue sections. *STAR Protoc*. 2022;3:101346.
43. Honda M, Oki S, Kimura R, et al. High-depth spatial transcriptome analysis by photo-isolation chemistry. *Nat Commun*. 2021;12:4416.
44. Maere S, Heymans K, Kuiper M. BiNGO: A cytoscape plugin to assess overrepresentation of gene ontology categories in biological networks. *Bioinformatics*. 2005;21:3448-3449.
45. Florio M, Albert M, Taverna E, et al. Human-specific gene *ARHGAP11B* promotes basal progenitor amplification and neocortex expansion. *Science*. 2015;347:1465-1470.
46. Liberzon A, Birger C, Thorvaldsdottir H, Ghandi M, Mesirov JP, Tamayo P. The molecular signatures database (MSigDB) hallmark gene set collection. *Cell Syst*. 2015;1:417-425.
47. Liberzon A, Subramanian A, Pinchback R, Thorvaldsdottir H, Tamayo P, Mesirov JP. Molecular signatures database (MSigDB) 3.0. *Bioinformatics*. 2011;27:1739-1740.
48. Schaefer CF, Anthony K, Krupa S, et al. PID: The pathway interaction database. *Nucleic Acids Res*. 2009;37(Database issue): D674-D679.
49. Tanaka Y, Shimanaka Y, Caddeo A, et al. LPIAT1/MBOAT7 depletion increases triglyceride synthesis fueled by high phosphatidylinositol turnover. *Gut*. 2021;70:180-193.
50. Bligh EG, Dyer WJ. A rapid method of total lipid extraction and purification. *Can J Biochem Physiol*. 1959;37:911-917.
51. Bartlett GR. Phosphorus assay in column chromatography. *J Biol Chem*. 1959;234:466-468.
52. Sherry ST, Ward MH, Kholodov M, et al. dbSNP: The NCBI database of genetic variation. *Nucleic Acids Res*. 2001;29:308-311.
53. Fairley S, Lowy-Gallego E, Perry E, Flicek P. The international genome sample resource (IGSR) collection of open human genomic variation resources. *Nucleic Acids Res*. 2020;48(D1):D941-D947.
54. Tadaka S, Hishinuma E, Komaki S, et al. jMorp updates in 2020: Large enhancement of multi-omics data resources on the general Japanese population. *Nucleic Acids Res*. 2021;49(D1):D536-D544.
55. Karczewski KJ, Francioli LC, Tiao G, et al. The mutational constraint spectrum quantified from variation in 141,456 humans. *Nature*. 2020;581:434-443.
56. Jaganathan K, Kyriazopoulou Panagiotopoulou S, McRae JF, et al. Predicting splicing from primary sequence with deep learning. *Cell*. 2019;176:535-548.e24.
57. Chicco AJ, Sparagna GC. Role of cardiolipin alterations in mitochondrial dysfunction and disease. *Am J Physiol Cell Physiol*. 2007;292:C33-C44.
58. Lancaster MA, Renner M, Martin CA, et al. Cerebral organoids model human brain development and microcephaly. *Nature*. 2013;501:373-379.
59. Pasca AM, Sloan SA, Clarke LE, et al. Functional cortical neurons and astrocytes from human pluripotent stem cells in 3D culture. *Nat Methods*. 2015;12:671-678.
60. Di Lullo E, Kriegstein AR. The use of brain organoids to investigate neural development and disease. *Nat Rev Neurosci*. 2017;18: 573-584.

61. Martinez-Cerdeno V, Noctor SC. Neural progenitor cell terminology. *Front Neuroanat*. 2018;12:104.
62. Kalebic N, Gilardi C, Stepien B, et al. Neocortical expansion due to increased proliferation of basal progenitors is linked to changes in their morphology. *Cell Stem Cell*. 2019;24:535-550.e9.
63. Kostic M, Paridaen JTML, Long KR, et al. YAP activity is necessary and sufficient for basal progenitor abundance and proliferation in the developing neocortex. *Cell Rep*. 2019;27:1103-1118.e6.
64. Uzquiano A, Gladwyn-Ng I, Nguyen L, et al. Cortical progenitor biology: Key features mediating proliferation versus differentiation. *J Neurochem*. 2018;146:500-525.
65. Ohnuki M, Takahashi K, Yamanaka S. Generation and characterization of human induced pluripotent stem cells. *Curr Protoc Stem Cell Biol*. 2009;Chapter 4:Unit 4A 2.
66. Zhao J, Fu Y, Yamazaki Y, et al. *APOE4* exacerbates synapse loss and neurodegeneration in Alzheimer's disease patient iPSC-derived cerebral organoids. *Nat Commun*. 2020;11:5540.
67. Bershteyn M, Nowakowski TJ, Pollen AA, et al. Human iPSC-derived cerebral organoids model cellular features of lissencephaly and reveal prolonged mitosis of outer radial glia. *Cell Stem Cell*. 2017;20:435-449.e4.
68. Khacho M, Harris R, Slack RS. Mitochondria as central regulators of neural stem cell fate and cognitive function. *Nat Rev Neurosci*. 2019;20:34-48.
69. Malatesta P, Appolloni I, Calzolari F. Radial glia and neural stem cells. *Cell Tissue Res*. 2008;331:165-178.
70. Tomooka Y, Kitani H, Jing N, Matsushima M, Sakakura T. Reconstruction of neural tube-like structures in vitro from primary neural precursor cells. *Proc Natl Acad Sci U S A*. 1993;90:9683-9687.
71. Subramanian A, Tamayo P, Mootha VK, et al. Gene set enrichment analysis: A knowledge-based approach for interpreting genome-wide expression profiles. *Proc Natl Acad Sci U S A*. 2005;102:15545-15550.
72. Merico D, Isserlin R, Stueker O, Emili A, Bader GD. Enrichment map: A network-based method for gene-set enrichment visualization and interpretation. *PLoS One*. 2010;5:e13984.
73. Bretones G, Delgado MD, Leon J. Myc and cell cycle control. *Biochim Biophys Acta*. 2015;1849:506-516.
74. Zinin N, Adameyko I, Wilhelm M, et al. MYC proteins promote neuronal differentiation by controlling the mode of progenitor cell division. *EMBO Rep*. 2014;15:383-391.
75. Iwata R, Vanderhaeghen P. Regulatory roles of mitochondria and metabolism in neurogenesis. *Curr Opin Neurobiol*. 2021;69:231-240.
76. Khacho M, Slack RS. Mitochondrial dynamics in the regulation of neurogenesis: From development to the adult brain. *Dev Dyn*. 2018;247:47-53.
77. Fan X, Fu Y, Zhou X, et al. Single-cell transcriptome analysis reveals cell lineage specification in temporal-spatial patterns in human cortical development. *Sci Adv*. 2020;6:eaaz2978.
78. Dehay C, Kennedy H. Cell-cycle control and cortical development. *Nat Rev Neurosci*. 2007;8:438-450.
79. Geraldo LHM, Spohr T, Amaral RFD, et al. Role of lysophosphatidic acid and its receptors in health and disease: Novel therapeutic strategies. *Signal Transduct Target Ther*. 2021;6:45.
80. Noguchi K, Herr D, Mutoh T, Chun J. Lysophosphatidic acid (LPA) and its receptors. *Curr Opin Pharmacol*. 2009;9:15-23.
81. Kingsbury MA, Rehen SK, Contos JJ, Higgins CM, Chun J. Non-proliferative effects of lysophosphatidic acid enhance cortical growth and folding. *Nat Neurosci*. 2003;6:1292-1299.
82. Supek F, Lehner B, Lindeboom RGH. To NMD or not to NMD: Nonsense-mediated mRNA decay in cancer and other genetic diseases. *Trends Genet*. 2021;37:657-668.
83. Chai G, Webb A, Li C, et al. Mutations in spliceosomal genes *PPIL1* and *PRP17* cause neurodegenerative pontocerebellar hypoplasia with microcephaly. *Neuron*. 2021;109:241-256.e9.
84. Thompson K, Bianchi L, Rastelli F, et al. Biallelic variants in *TAMM41* are associated with low muscle cardiolipin levels, leading to neonatal mitochondrial disease. *HGG Adv*. 2022;3:100097.
85. Nowakowski TJ, Pollen AA, Sandoval-Espinosa C, Kriegstein AR. Transformation of the radial glia scaffold demarcates two stages of human cerebral cortex development. *Neuron*. 2016;91:1219-1227.
86. Bartek J, Lukas C, Lukas J. Checking on DNA damage in S phase. *Nat Rev Mol Cell Biol*. 2004;5:792-804.
87. Pollen AA, Nowakowski TJ, Chen J, et al. Molecular identity of human outer radial glia during cortical development. *Cell*. 2015;163:55-67.
88. Murakami M, Sato H, Taketomi Y. Updating phospholipase A_2 biology. *Biomolecules*. 2020;10:1457.
89. Shindou H, Shimizu T. Acyl-CoA:lysophospholipid acyltransferases. *J Biol Chem*. 2009;284:1-5.
90. Pinson A, Xing L, Namba T, et al. Human TKTL1 implies greater neurogenesis in frontal neocortex of modern humans than Neanderthals. *Science*. 2022;377:eabl6422.